2021년 2월
석사학위 논문

Electrochemical lithium storage behavior of 3D porous architecture for rechargeable lithium batteries

조선대학교 대학원

첨단소재공학과

윤 종 혁

Electrochemical lithium storage behavior of 3D porous architecture for rechargeable lithium batteries

리튬이차전지용 3차원 다공성 구조체 전극의
전기화학적 리튬 저장 거동 해석

2021년 2월 25일

조선대학교 대학원

첨단소재공학과

윤 종 혁

Electrochemical lithium storage behavior of 3D porous architecture for rechargeable lithium batteries

지도교수   강 현 철

논문을 공학 석사학위신청 논문으로 제출함

2020년 10월

조선대학교 대학원

첨단소재공학과

윤 종 혁

윤종혁의 석사학위논문을 인준함

위원장　조선대학교 교 수　　이 종 국　(인)

위 원　조선대학교 교 수　　신 동 찬　(인)

위 원　조선대학교 교 수　　강 현 철　(인)

2020 년　11 월

조선대학교 대학원

CONTENTS

List of Figures

ABSTRACT

Electrochemical lithium storage behavior of 3D porous architecture for rechargeable lithium batteries

Jonghyeok Yun

Advisor : Prof. Hyon Chol Kang

Dept. of Advanced Materials

Engineering, Graduate School of

Chosun University

Although Li-metal electrodes are able to enhance the energy density of rechargeable batteries, they are characterized by poor cycle lifetimes and safety concerns due to large volumetric changes and dendritic growth during repeated cycling. Three-dimensional (3D) porous architectures have attracted considerable interest as a solution to these challenges. They may serve as lithium-metal electrodes for next-generation batteries with high energy densities. The high surface areas and large pore volumes of the 3D architecture electrode are useful in reducing local current density and suppressing significant volumetric changes during cycling. However, there are still issues with uncontrolled Li plating on top of the architecture electrode (top plating) for high energy density and long cycle lifetime Li-metal electrodes. This study proposes a synergistic surface activation-passivation of 3D-Cu architectures. It also puts forwards design of 3D framework electrodes with an interfacial activity gradient (IAG), on a kinetics-based mechanistic analysis of Li plating. Theoretical simulation demonstrated that an IAG design (i.e., increasing the activity for Li^+ reduction with increasing pore depth), assists the bottom-up growth of Li even without strict optimization of porous structures. This was demonstrated experimentally using model

architectures with effective interfacial properties. Synergistic surface activation‑passivation provides for efficient and robust Li-metal electrodes. A lithiophilic Ag nano-layer displaced *via* galvanic displacement activated Li nucleation over the entire 3D-Cu surface, while an inert, non-conductive Al_2O_3 coating passivates the top surface of 3D-Cu. This produced uniform Li on the porous architecture and controlled Li plating on top of the framework. The synergistic surface adjustment provides for high coulombic efficiency (>98%) and stable cycling performance without requiring the optimization of the porous architecture. This confirmed the uniform and reversible Li plating‑stripping from within the 3D-Cu architecture. Compared to conventional Cu architecture with a uniform interfacial activity, the IAG-Cu architecture electrode significantly improved morphological stability during high-capacity Li storage (40 mA h cm^{-2}), and reversibility during repeated Li plating‑stripping processes. The outcomes of this study provide basic insights into the design and construction of 3D framework electrodes to improve the cycling stability of rechargeable Li-metal batteries.

ABSTRACT

리튬이차전지용 3차원 다공성 구조체 전극의 전기화학 리튬 저장 거동 해석

Jonghyeok Yun

Advisor : Prof. Hyon Chol Kang

Dept. of Advanced Materials

Engineering, Graduate School of

Chosun University

리튬 금속 전극은 충전식 배터리의 에너지 밀도를 높일 수 있지만 사이클링 수명이 짧고 반복적인 충·방전 과정 동안 큰 부피변화와 dendrite의 성장으로 인해 안전 문제가 발생한다. 이러한 문제를 해결하기 위해서 3차원 (3D) 다공성 구조체는 에너지 밀도가 높은 차세대 배터리 용 리튬금속 전극 소재로 상당한 관심을 받았다. 3D 구조체는 넓은 표면적과 큰 기공으로 인해 local current density를 줄여주고 반복적인 충·방전 과정 중 전극의 부피 변화를 억제한다. 하지만 구조체 상부 표면에 제어되지 않은 리튬 plating 현상으로 인해 높은 에너지 밀도와 긴 수명에 대한 문제가 아직 해결이 되지 않았다. 본 논문에서는 이론 시뮬레이션 결과를 바탕으로 3D 구조체의 표면을 Activation, Passivation 시킨 Interfacial Activity Gradient (IAG) 디자인을 제안한다. 이론적 시뮬레이션 결과 IAG (기공 깊이 방향으로 리튬 이온 환원을 위한 표면 활성화 증가) 디자인을 통해 구조체의 기공 조절 없이 bottom-up 방식의 리튬 plating을 유도하는 결과를 확인하였다. 이는 모델 구조체를 사용하여 실험적으로 검증하였으며 구조체 표면의 Activation, Passivation은 효율적이고 안정적인 리튬 저장을 유도 할 수 있었다. Galvanic displacement 방법을 통해 코팅된 silver는 구조체 표면에서 Li 핵생성을 활성화 시키는 반면 비전도성 물질인 알루미나, PVdF 코팅은 구조체 표면에 코팅되어 리튬 전착을 물리적으로 제한하고 구조체 내부로의 균일한 plating을 유도 한다. 이러한 구조체는 미세

구조 조절없이 높은 쿨롱 효율 (>98%)과 안정적인 사이클링 성능을 제공한다. 이를 바탕으로 3차원 구조체 내부에서 균일하고 가역적인 리튬 plating, stripping 거동을 확인하였다. 또한 IAG 3D-Cu 구조체의 경우 고용량 (40 mA h cm^{-2}) 저장 동안 구조적 안정성과 반복적인 리튬 plating, stirrping 가역성이 크게 향상됨을 확인하였다. 본 논문은 3D 구조체 전극의 설계 및 디자인에 대한 기본적인 가이드라인을 제공하여 리튬금속 배터리의 사이클링 안정성을 개선하였다.

I. Introduction

Lithium-ion batteries (LIBs) have been widely adopted as power sources for electric vehicles and energy storage systems [1,2]. LIBs using graphite anodes (theoretical specific capacity of 372 mA h g^{-1}) have almost reached their theoretical specific energy density (350 W h kg^{-1}), although they are still unable to provide the high energy density required in long-range electric vehicles. There has been significant focus on Li-metal anodes as alternatives to graphite due to their low redox potential (-3.04 V *vs.* standard hydrogen electrode (SHE)) and high specific capacity (3860 mA h g^{-1}) [3-5]. This means that Li-metal electrodes can improve the energy density of LIBs and promote electrification of transport requiring high energy density batteries [6-8]. Despite this potential, there are three key issues that need to be addressed prior to the application of Li-metal anodes in rechargeable Li-metal batteries. First, the growth of uncontrollable Li-metal dendrites pose serious safety problems. Second, Li dendrites continue to grow on metal surfaces, especially at high currents, due to the increased Li$^+$ flux around the tips of the growing [9-11]. Third, when the Li-metal becomes thermodynamically unstable due to the high Fermi level, it triggers an irreversible and continuous reaction between Li and the electrolyte. This results in the formation of a thick solid electrolyte interphase (SEI) layer on the surface of the Li-metal [12]. Li-metal experiences a large volumetric (thickness) change during Li plating and stripping; however, the frailty of the SEI films renders them unable to completely suppress such a large change in the Li-metal electrode [13-22].

Recently, two-dimensional (2D) Cu foil has been used as a substrate (acting as a current collector) for Li-metal anodes because of its chemical/electrochemical stability to Li, and excellent processability for mass production.

In this regard, recent research has focused on two key aspects: (1) microstructural engineering, and (2) lithiophilic surface treatment. Hierarchical porous structures have been constructed for microstructural engineering. Recently, the focus has shifted to the design of three-dimensional (3D) Cu frameworks that do not experience macroscopic volumetric changes upon Li plating and stripping. Plated Li species will peel off when in the internal pores of the architecture. In addition, the effective Li^+ flux (current density) on the surface mitigates for uncontrolled growth of Li dendrites [23, 24]. For surface treatment, the entire architecture surface is modified with various lithiophilic elements that promote interfacial kinetics [25-28]. To date, there is insufficient research considering the complex nature of Li plating in 3D architecture electrodes, where Li^+ transport and interfacial reactions dynamically compete with each other. This is considered a critical scientific foundation to help develop a strategy that addresses the top growth problems.

This study proposes a combination of theoretical modeling and experimental studies that demonstrate the manipulation of the Li growth pattern in the 3D architecture electrode via spatial grading of interfacial activity. This proposed approach was devised to solve address two key intrinsic problems with 3D-Cu: (1) the large overpotentials exhibited by Cu for Li nucleation, and (2) the Li^+ transport limitation in the electrolyte-filled pores of the 3D architecture, producing uneven Li plating in 3D-Cu. The surface activity of Cu was adjusted using Ag for activation or insulative polyvinylidene fluoride (PVdF) or Al_2O_3 (AO) for passivation. The surface conditioning electrode has the following unique features that enable uniform Li plating.

Ⅱ. Literature survey

A. Li-ion battery

Li-ion rechargeable batteries have enabled the wireless revolution of mobile phones, laptop, and digital cameras, facilitating global communication. Graphite-$LiCoO_2$ has now become the leading Li-ion battery system that powers most portable electronic devices.

Figure. 1 presents the basic Li-ion battery system that has led to the current battery market. The main cell reaction is the reversible Li-ion intercalation/de-intercalation cycle between two layered compounds. To ensure the anodic stability of the cathode material and electrolyte solutions, the cathode reaction is as follows:

$$LiCoO_2 \leftrightarrow Li_{1-x}CoO_2 + xLi^+ + xe^-$$

The first process in the cell is constantly charging; $LiCoO_2$ is oxidized and delithiated in parallel with the reduction and lithiation of graphite. Graphite reversibly intercalates with lithium to form LiC_6 as the final product according to the following reaction:

$$C_6 + xLi^+ + xe^- \leftrightarrow Li_xC_6$$
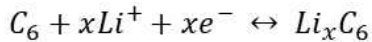
The graphite anode is widely as a major obstacle, preventing the application of LIBs at high charge rates. This has been attributed to its low operating potential and slow kinetics for Li^+ intercalation. In addition, Li plating on the surface of graphite is potentially risky as it may subsequently lead to poor LIB performance and thermal runaway.
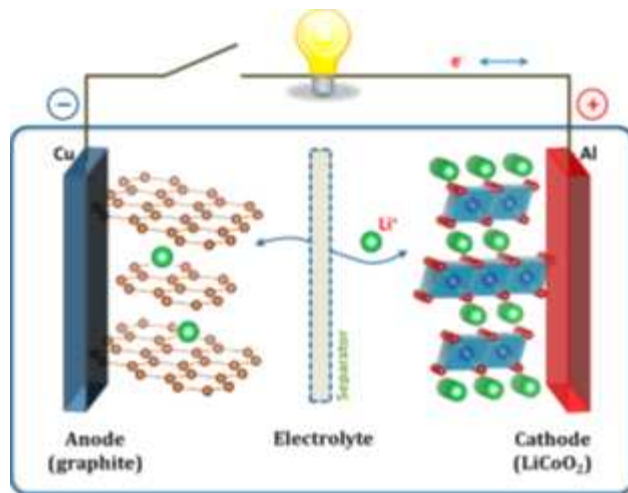
Figure 1. Schematic illustration of the first Li-ion battery (LiCoO2/Li^{+}electrolyte/graphite) [1].

B. Next generation batteries

1. Lithium metal based batteries

Li-metal based batteries have much higher weight and volumetric energy density than traditional Li-ion batteries; as such, considerable effort has been directed toward developing Li-S or Li-air for large-scale power storage systems. Figure. 2 illustrates the basic Li-metal, Li-air, and Li-S battery systems. Li-metal batteries that use Li-metal anodes may be classified into three groups: (1) an Li-air battery with O_2 reduction as the cathode; (2) an Li-S battery with sulfur as the cathode; and (3) a Li-metal battery with an intercalation cathode [2]. However, there are two significant challenges facing the development of Li-metal anodes. First, Li-metal experiences large volumetric changes during Li plating and stripping; and second, once formed, the Li^+ flux around the tip of the growing dendrite increases, such that the Li dendrite continues to grow on the metal surface, particularly at high currents [29].

2. Lithium metal related issues

a. Lithium plating-stripping process

Figure. 3(b) presents the Li plating and stripping process. During Li plating, large volumetric expansion causes the fragile SEI to burst (step 1) and promotes the growth of Li dendrites through cracks (step 2). During Li stripping, volumetric shrinkage further destroys the SEI, and twisting of the stripping foam from within or at its root disrupts electrical contact and produces 'dead' Li (step 3). Following the continuous cycling (step 4), the repetition of the process produces a porous Li electrode, a thick accumulated SEI layer, and excessive dead Li. This causes the blockage of ion transport and reduced capacity. Further detailed correlations are summarized in Figure. 3(c).

b. Large volume change

Alloy-type anodes undergo a much larger volumetric change (~400% for Si), which is an obstacle for commercialization. Due to its hostless nature, the relative volumetric change of an Li anode is virtually infinite. The growth of Li dendrites and the deposition of porous Li exacerbates the volumetric change issues. From a practical point of view, the area capacitance of a single-sided commercial electrode should be a minimum of 3 mA h cm^{-2}.ThiscorrespondstoarelativechangeinthethicknessofLi [28, 30] of approximately 15 μm. For batteries, this minimum may be even higher, and essentially means that the movement of the Li interface during cycling may be tens of micrometers. This poses a major challenge in terms of achieving SEI stability.

c. Formation of Li dendrite and dead Li

Figure. 3(a) presents the typical dendritic Li morphology obtained from the Li/gel polymer electrolyte/LiMn$_2$O$_4$ cell following one cycle [31, 32]. The formed Li dendrite is able to directly contact the positive electrode, causing an internal short circuit and spontaneous rapid discharge of the battery.

The formation of dead Li inside the cell paralyzes the battery. Small Li particles or filaments detach from the substrate and are compactly wrapped by an electronically insulating SEI layer to form dead Li. Once dead Li is formed, it cannot be reversed into active Li. As it participates in the plating and stripping procedures, there is a loss of Li sources with gradually intensified capacity-fading [28].

d. Cell short circuit form Li dendrite

The heterogeneous deposition from large polarization and strong electric fields tends to cause dendrite nucleation. The next unlimited growth can cause severe short circuits, fires, or explosions in Li-metal batteries [11, 28, 31].

To address these issues with Li-metal anodes, there has been tremendous effort directed toward controlling the growth of Li dendrites and stabilizing the SEI. Various electrolyte additives have been used to improve the stability of the SEI layer. Solid and gel electrolytes with a high shear modulus have also been used to suppress the growth of Li dendrites.

3. 3D framework

To date, there has been a considerable research effort devoted to mitigating the dendritic growth of metallic Li. In particular, metallic Li storage in the 3D framework electrodes is considered effective in solving the problems caused by dendrites. Various current collector hosts, such as a 3D framework with a submicron skeleton, 3D porous copper, 3D graphene/metal scaffolds, and free-standing Cu nanowire networks, have been used to host Li metals using an electrodeposition approach. The large surface area and high porosity of the 3D framework electrode offers it the ability to confine metallic Li within the porous structure. This reduces local current densities and improves resistance to column changes. However, the electrodeposition approach to preserve Li, manipulated by assembling the host and bare Li foil into a working cell, generally causes non-uniform Li deposition. This is because most Li metals prefer to be plated on top of the host network due to ionic resistance. Figure. 4 shows that the number of electrolyte-filled pores suppresses the transfer of Li^+ to the bottom of the electrode. Contrary to common expectations, 3D architecture electrodes have poor cycle stability and tend to indicate premature cell failure in normal and high current operations [23, 24, 33, 34].

Recently, reported that some elements (e.g., Au, Ag, Zn) share a strong binding energy with Li-metal, which highlights a lithiophilic nature. When sputtering these lithiophilic layers on Cu foil, Li-metal prefers to nucleate on the lithiophilic region as opposed to the lithiophobic Cu region [35].
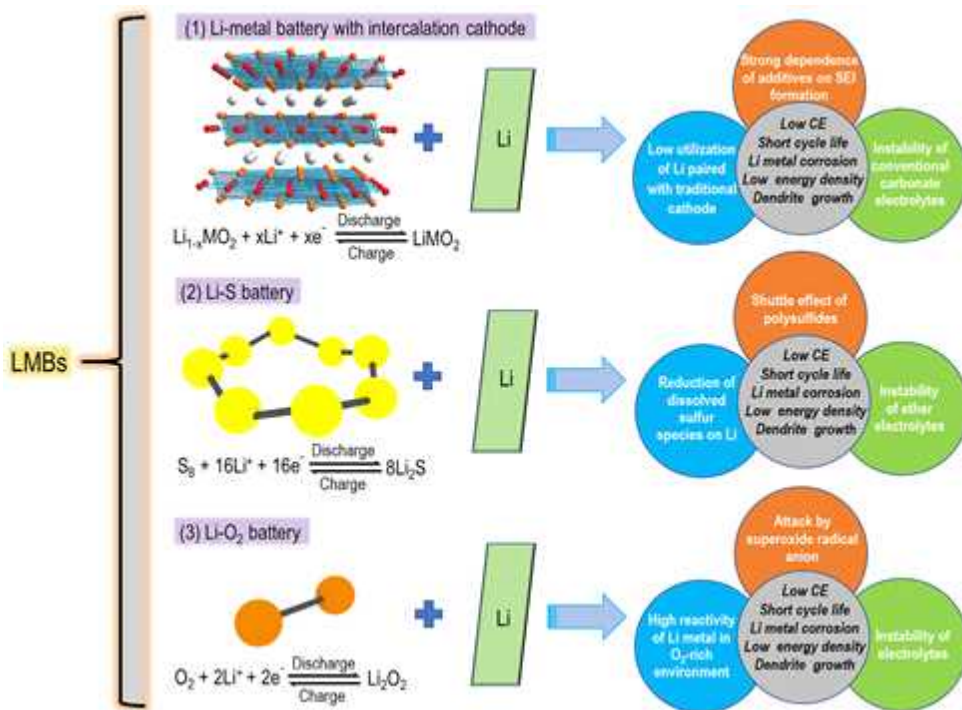
Figure 2. Overview of Characteristics of the Li Metal Battery Family and Challenges Facing Li Metal Anodes [2].
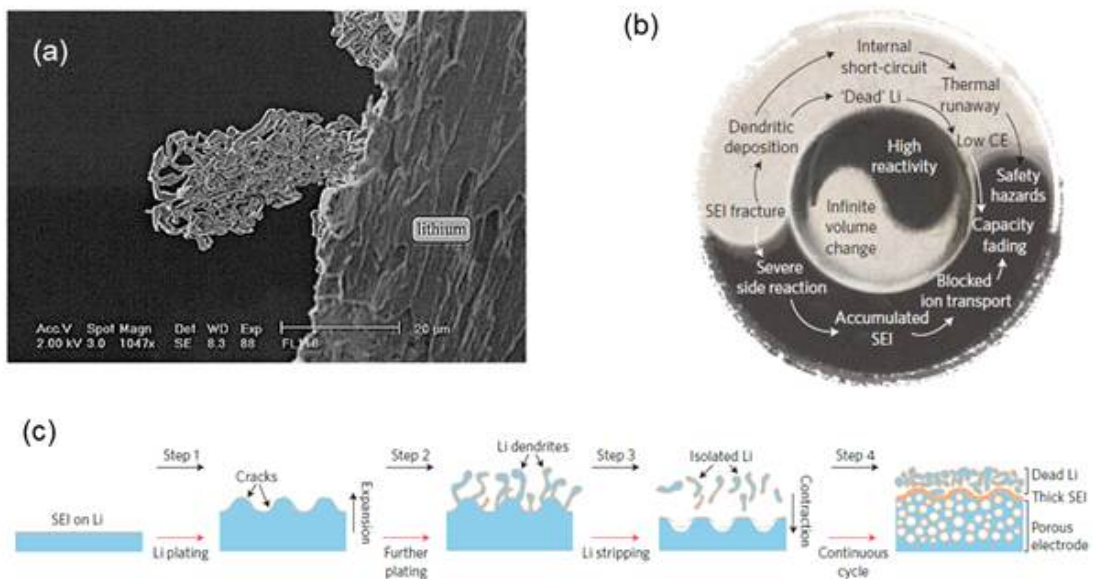
Figure 3. (a) Dendritic Li formed in a Li battery after charge at 2.2 mA cm^{-2} (Science Direct, reprinted with permission), (b) Correlations among the different challenges in the Li metal anode, originating from high reactivity and infinite relative volume change, (c) Schematic showing the Li stripping/plating process [27, 30].
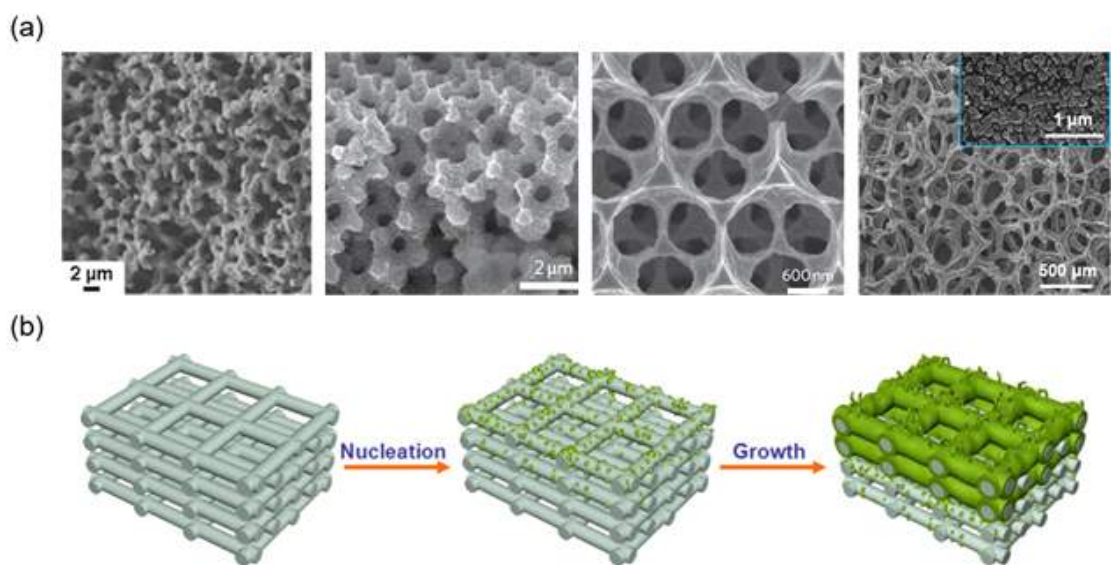
Figure 4. (a) 3D current collectors and composite electrode prepared by template methods [32]. (b) Schematic diagram of lithium nucleation and growth in the host [33].

Ⅲ. Synergistic surface activation-passivation of porous architecture

A. Experimental methods

1. Materials synthesis

This study used commercially available Cu foam (thickness = 1.0 mm; MTI Korea), that was uniaxially pressed to reduce its thickness to 500 m. Cu foam was sonicated in a 30% ethanol solution for 2 min and washed with deionized water to remove organic residues. It was then immersed in excess acetic acid (99.5%, Samchun) at 35 °C for 5 min and rinsed with deionized water to remove the native oxide. The galvanic displacement (GD) solution consisted of 59 mM $AgNO_3$ (99.9%, Samchun), 0.58 M $(NH_4)_2SO_4$ (99.0%, Samcun), and 3.78 M NH_4OH (28.0%,Sigma-Aldrich). Prior to GD, the solution was completely purged with N_2 gas for 30 min. To prepare the 3D-Cu@Ag, a Cu foam was immersed in the GD solution, followed by washing with deionized water and ethanol, and drying overnight in a vacuum. The 3D-Cu@Ag|AO was prepared by brush-coating the top surface of the 3D-Cu@Ag with an Al_2O_3 slurry. The coating slurry was prepared by mixing Al_2O_3 nanopowder (90 wt.%) and a binder (10 wt.% PVdF) in a N-methyl-2-pyrrolidone (NMP) solution.

2. Materials characterizations

The crystal structures of the prepared materials were characterized using X-ray diffraction (XRD) recorded on an automatic Rigaku diffractometer (2500 D/MAX, Rigaku) using Cu K$_\alpha$ radiation. Surface chemistry was investigated by X-ray photoelectron spectroscopy (XPS, Thermo Scientific, Sigma Probe). The sample morphology, microstructure, and composition were examined using scanning electron microscopy (SEM; Hitachi S-4800) in combination with energy-dispersive X-ray spectroscopy (EDS).

3. Electrochemical experiments

Electrochemical tests were conducted using a coin-type cell (CR-2032) with an Li-metal counter electrode and a polypropylene separator (Celgard 3501). The diameters of the 3D architecture (working) and Li (counter) electrodes were 1.675 and 1.615 cm, respectively. The electrolyte consisted of 1 M lithium bis(trifluoromethanesulfonyl)imide (LiTFSI) in a mixture of 1,3-dioxolane (DOL) and 1,2-dimethoxyethane (DME) (1:1 by volume) with 1 wt.% $LiNO_3$. Li plating was conducted with either 2.0, 5.0, or 20 mA h cm^{-2} at 0.5 mA cm^{-2}. Cycling tests were conducted with 1.0 mA g cm^{-2} at 1.0 mA cm^{-2} until cell voltage reached 1.5 V $vs.$ Li/Li$^+$. The current transient experiments were conducted using a Bio-Logic SP-200 in a three-electrode cell with an Li reference and counter electrode. The cell was initially held at 0.1 V $vs.$ Li/Li$^+$for , and then current transients were measured by reducing the voltage to -0.2 V $vs.$ Li/Li$^+$.

For full cell preparation, a cathode slurry was prepared by mixing the active material (80 wt.%, LiFePO$_4$), conductive agent (10 wt.%, Super-P), and binder (10 wt.%, PVdF) in an NMP solution. The slurry was coated on an Al foil and subsequently dried under vacuum at 120 ℃ for 12 h. Finally, electrodes were pressed with a twin roller. The full cell was designed and constructed with an areal capacity of ~1.0 mA h cm^{-2}, , and were charged and discharged for a voltage range of 2.0-4.0 V at current densities ranging from 0.5 to 5.0 cm^{-2}. The entire cell assembly was conducted in an argon-filled glove box. Unless otherwise stated, all electrochemical measurements were taken at 25 ℃ using a battery tester (WonATech, WBCS3000S).

B. Result and discussion

1. Surface activation of 3D-Cu architectures *via* galvanic displacement of Ag and Cu

Ag nanolayers were deposited on the 3D-Cu using a simple and controlled GD process. Commercially available Cu foam was dipped in a solution consisting of $AgNO_3$ and excess NH_3.Inthepresenceof excess NH_3, Ag^+ is known to bind to NH_3 to form $[Ag(NH_3)_2]^+$ complex cations with a redox potential of 0.373 V *vs.* SHE [36, 37]. The GD reaction was driven by the redox potential difference between $[Ag(NH_3)_2]^+$ and Cu^{2+} (0.34 V *vs.* SHE), that is, $[Ag(NH_3)_2]^+$ cations were reduced to Ag(s), while Cu(s) was oxidized to $[Cu(NH_3)4]^{2+}$ complex cations:

$$2[Ag(NH_3)_2]^+ + Cu(s) \rightarrow 2Ag(s) + [Cu(NH_3)_4]^{2+} \tag{1}$$
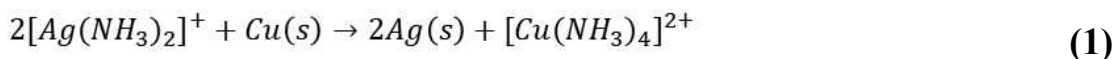
Following the GD process, the entire 3D-Cu surface was covered with a white Ag layer, as shown in Figure. 5(a). When the GD process had commenced, the colorless $AgNO_3$-NH_3 solution changed to blue, darkening with increasing GD time (t_{GD}), indicating an increased amount of $[Cu(NH_3)_4]^{2+}$.

Figure. 5(b) shows the XRD patterns of 3D-Cu@Ag exposed to GD for various t_{GD}.The XRD data shows characteristic diffraction peaks for Cu (JCPDS no.04-0836) at 43.3° (111) and 50.4° (200), and the peaks of Ag (JCPDS no. 04-0783) at 38.1° (111), 44.3° (200), and 64.4° (220). With the progression of the GD process, the Ag intensities deposited on the Cu surface had increased. The formation of GD-derived Ag deposits was also confirmed by EDS (Figure. 6(a)).

XPS analysis was conducted to obtain detailed information on the surface chemistry of 3D-Cu@Ag, as shown in Figure. 5(c). The XPS profiles of 3D-Cu@Ag with t_{GD} at 10 and 15 s show that the Ag $3d_{5/2}$ and $3d_{3/2}$ peaks had binding energies of 368.3 and 374.3 eV, respectively, demonstrating that the GD-derived Ag deposits were mainly metallic. [38].

The SEM imagery of 3D-Cu in Figure 7(a) and (b) shows that Cu strips that were 60-90 m wide were interwoven with each other, producing a porosity similar to that of 3D-Cu, regardless of the t_{GD} (Figure. 6); this means microstructure of the 3D architecture was stored in the GD of Ag. The SEM imagery of the surface morphology following the commencement of GD, Ag nanoparticles were formed for the extension of GD, that is, t_{GD} = 60 s (Figure. 7(f), inset)

Figure. 7(g)−(i) shows the cross-sectional SEM imagery of 3D-Cu@Ag for t_{GD} = 10 s and the corresponding EDS mapping of Ag. Samples were prepared via cross-section milling (Ar$^+$ beam). The Cu strip was coated with a conformal, pore-free Ag layer, and the interface between Ag and Cu was cohesive, showing no signs of cracking or delamination. Top surface SEM and EDS analyses confirmed the uniform distribution of Ag on 3D-Cu@Ag (Figure. 8). The thickness of Ag was estimated to be ~400 nm at t_{GD} = 10 s and increased to ~715 nm at t_{GD} =15 s (Figure. 8(c)). As this study was focused on the surface modification of 3D-Cu with Ag as opposed to bulky Ag deposition, the 3D-Cu@Ag with t_{GD} = 10 s was selected for the subsequent experiments.
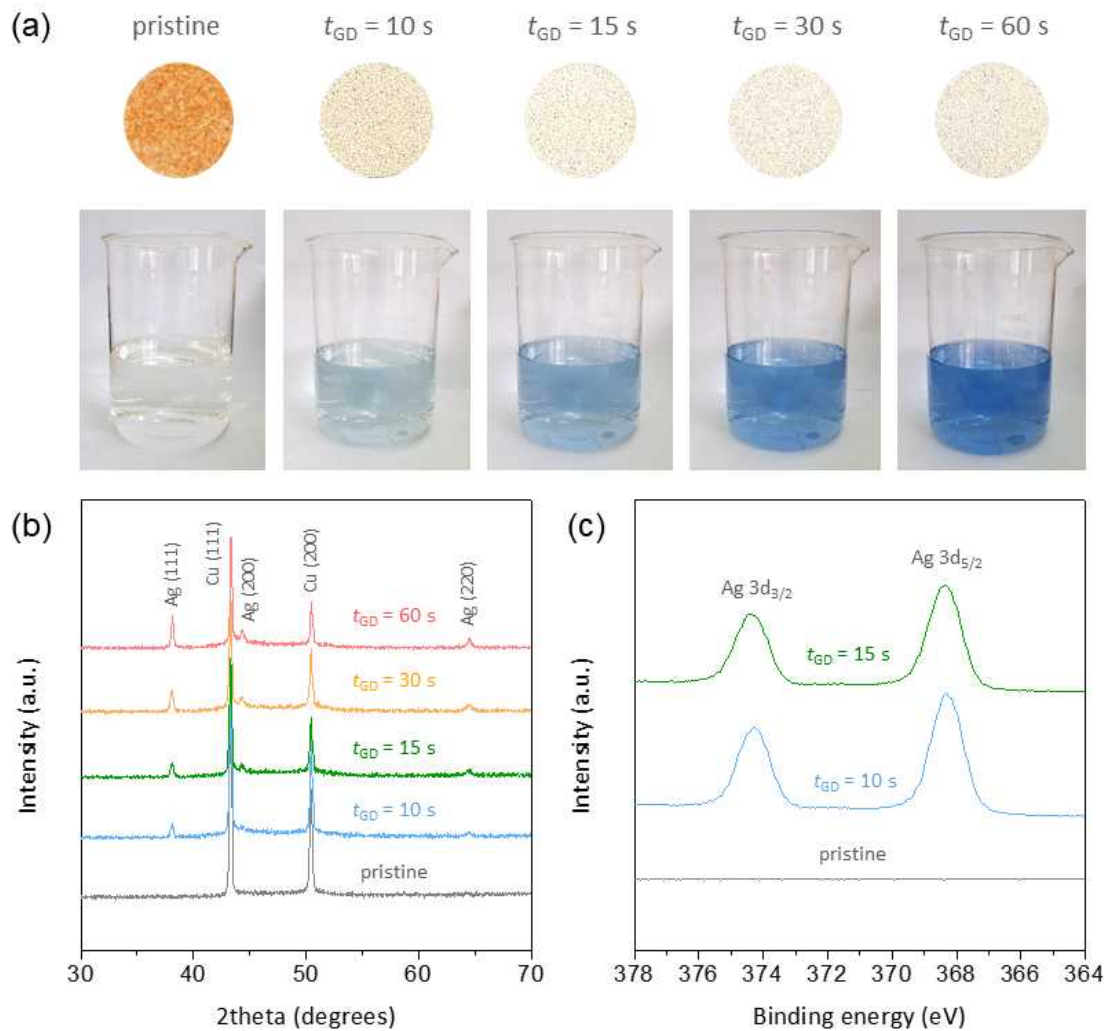
Figure 5. (a) Photographs of 3D-Cu architecture and the solutions taken after the GD processes for various t_{GD}. (b) XRD patterns and (c) XPS Ag 3d spectra of 3D-Cu and 3D-Cu@Ag [21].
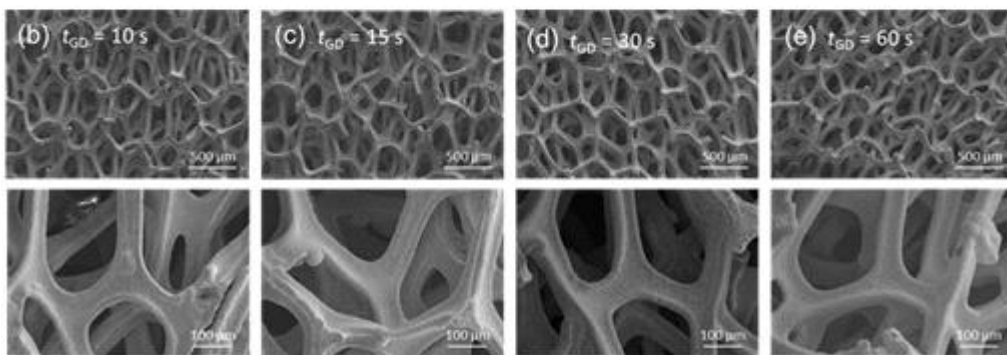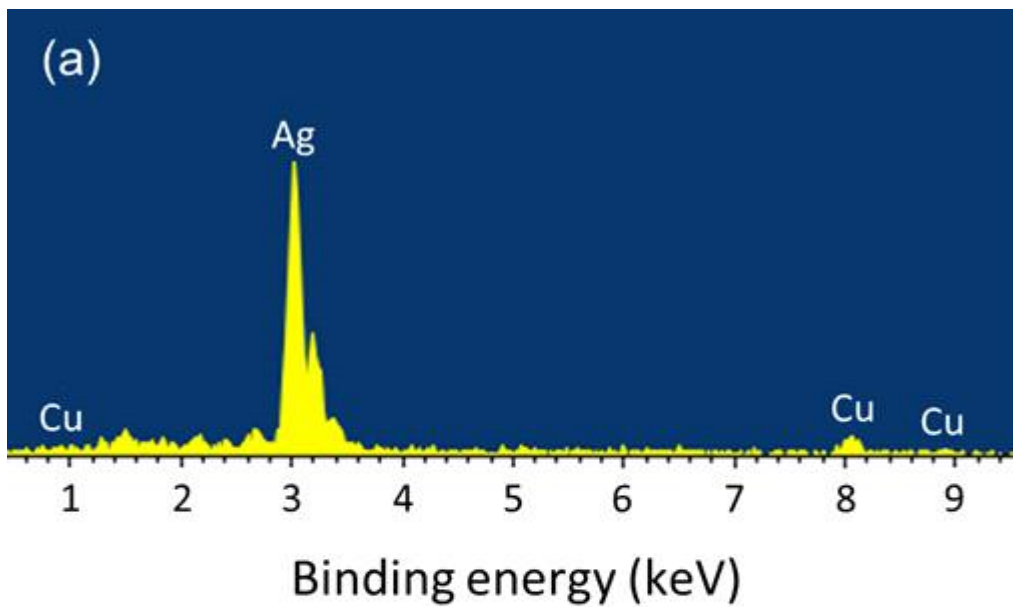
Figure 6. (a) EDS spectrum of 3D-Cu@Ag subjected to GD for t_{GD} = 10 s [21]. Low-magnification SEM images of 3D-Cu@Ag architectures for (b) t_{GD} = 10 s, (c) t_{GD} = 15 s, (d) t_{GD} = 30 s, (e) t_{GD} = 60 s [21].
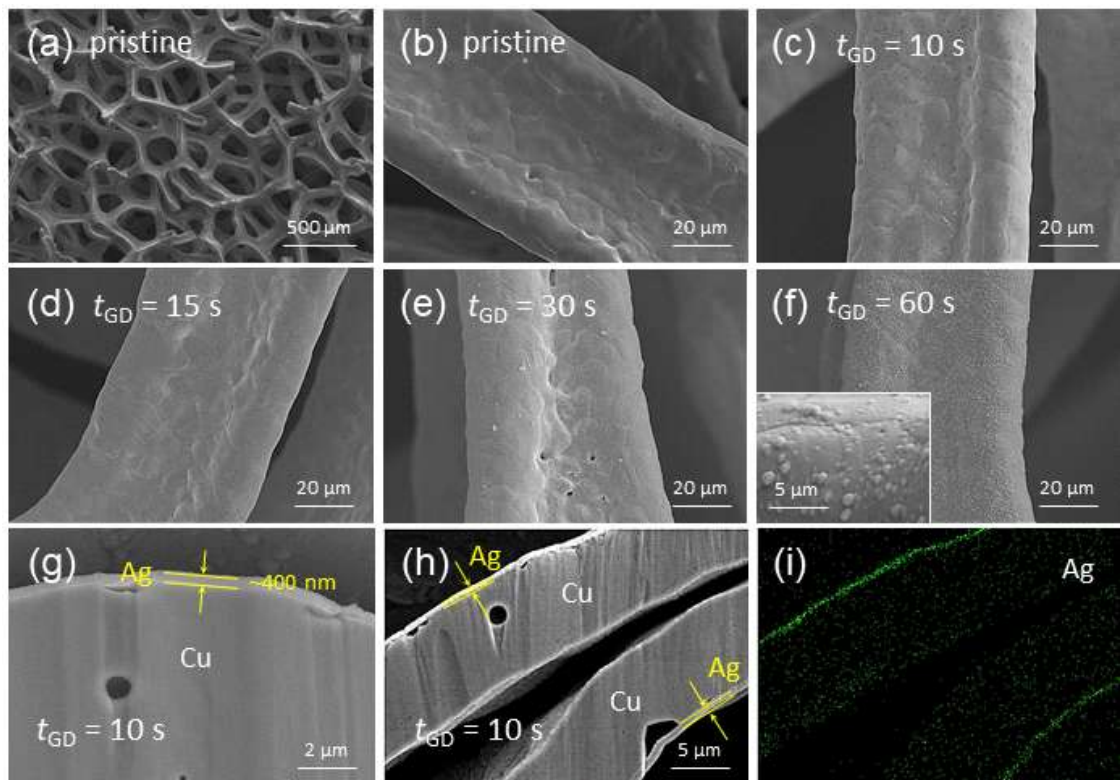
Figure 7. SEM images of (a and b) 3D-Cu and (c-f) 3D-Cu@Ag architectures for (c) t_{GD} = 10 s, (d) t_{GD} = 15 s, (e) t_{GD} = 30 s, (f) t_{GD} = 60 s. (g and h) Cross-sectional SEM images of 3D-Cu@Ag for t_{GD} = 10 s and (i) the corresponding EDS mapping result for Ag [21].
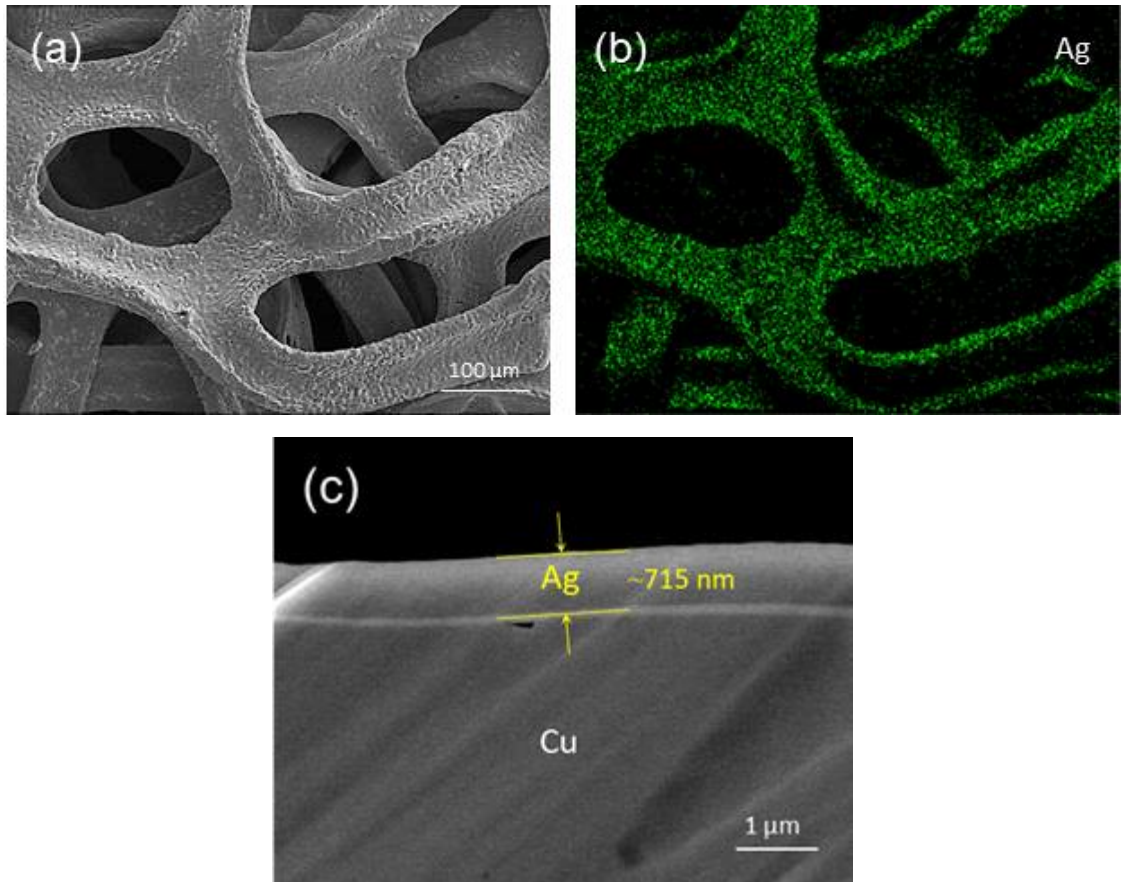
Figure 8. (a) SEM image (top view) of 3D-Cu@Ag for t_{GD} = 10 s and (b) the corresponding EDS mapping result for Ag, (c) Cross-sectional SEM image of 3D-Cu@Ag for t_{GD} = 15 s [21].

2. Li storage behavior of 3D-Cu@Ag architectures

To investigate the effect of GD-derived Ag on Li plating behavior, Li∥3D-Cu@Ag cells were assembled and tested at a constant current density of 0.5 mA cm^{-2}. For comparison, the same experiment was conducted using a 2D-Cu foil and a 3D-Cu architecture, where the 1 M LiTFSI in DOL:DME (1:1 in volume) with 1 wt.% LiNO$_3$ electrolyte was used. Figure 9 presents a comparison of the typical voltage profiles of the 3D-Cu and 3D-Cu@Ag electrodes recorded during Li plating with an areal capacity of 2.0 mA h cm^{-2}. The voltage profiles of 3D-Cu had a momentary voltage drop of approximately -0.1 V *vs.* Li/Li$^+$ at the moment of current application. The voltage then rapidly increases to a steady-state value. The 2D-Cu electrode behaved the same way as its 3D-Cu counterpart (Figure 10). This voltage drop has also been observed in previous studies [],indicating that an energy barrier must be overcome to form critically sized Li nuclei on the Cu substrate. High nucleation barriers are known to cause spatially heterogeneous Li nucleation on the 3D Cu surface [35]. However, there was no voltage drop for the 3D-Cu@Ag electrode during in the early stage of Li plating, although it did exhibit a monotonous voltage drop to a steady-state level. This indicates that GD-derived Ag dissolved into Li to form a Li–Ag solid solution in the early stages, acting as a buffer layer for further Li plating and eliminating the nucleation barriers.

To confirm the Ag-activated Li nucleation on 3D-Cu@Ag, Li plating kinetics were examined using potentiostatic current transient analysis (chronoamperometry) based on multiple nucleation with diffusion-controlled growth model [39-42]. Note that current transient measurements were conducted on 2D-Cu and 2D-Cu@Ag (Figure 10) to avoid the complexity resulting from the 3D architecture. A three-electrode cell with Li reference and counter electrodes was used for measurements. As shown in Figure. 9(b), the relationship between current density (*i*) versus time (*t*) (current transients) was obtained by applying a potential step from 0.1 to -0.2 V *vs.* Li/Li$^+$. We then analyzed this using a theoretical model developed by Scharifker and Mostany [39, 41]:

$$i(t) = zFc\left(\frac{D}{\pi t}\right)^{\frac{1}{2}}\left\{1 - \exp\left[-(2\pi)^{\frac{2}{3}}D\left(\frac{cM}{\rho}\right)^{\frac{1}{2}}\frac{N_o}{A}\left(At - 1 + \exp(-At)\right)\right]\right\}$$

(2)

where z is the number of electrons exchanged; F is the Faraday constant (96 485 C mol$^-$^{1}); c is the concentration of Li$^+$(1.0×10^{-3} mol cm^{-3}); D is the diffusion coefficient of Li$^+$ (2.0×10^{-10} cm^{2}s^{-1}) [43],)[]; M is the molar mass of Li (6.941 g mol^{-1}); ρ is the density of Li (0.534 g cm^{-3}); N_o is the nucleus density (number of active sites per cm^2);and$A$ is the nucleation rate (number of nuclei per active site per second). The current transients measured on Cu and Cu@Ag showed that the current had increased over time in the early stages of Li plating (region 1), and then gradually decayed (region 2). Hyde et al. [40] demonstrated that for the initial rising current transient (region 1), Eq. (2) reduces to:

$$i(t) = \left[2^{\frac{1}{2}}zFc\pi D^{\frac{3}{2}}\left(\frac{cM}{\rho}\right)^{\frac{1}{2}}N_oA\right]t^{\frac{3}{2}}$$

(3)

The nucleation rates, expressed as NoA (number of nuclei per cm^2 per second), were determined from fitting the measured current transients to as shown in Figure. 9(c). The value of NoA for Cu@Ag was 4.64 × 10^8 cm^8 cm^{-2} s^{-1}; this was much higher than Cu (1.27 × 10^8 cm^{-2} s^{-1}), and the beneficial role of GD-derived Ag was confirmed to enhance the Li nucleation rate.

The surface morphology of the 3D architecture electrodes was characterized following Li plating. The photograph of the 3D-Cu electrode (Figure. 9(d), inset) taken after the Li plating test showed white-colored deposits on the top surface (on the separator side). The SEM imagery of 3D-Cu (Figure 9(d) and (e)) obtained after Li plating (2.0 mA h cm^{-2} at 0.5 mA cm^{-2}) revealed preferential Li plating on top of 3D-Cu as opposed to within the 3D structure. High-resolution SEM imagery (Figure 9(e)) salso showed that surface deposits consisted of Li dendrites (filaments) that were several micrometers in diameter. Ex-situ observations (Figure 9(f) and (g)) for 3D-Cu@Ag showed that the coverage of Li deposits on the top surface was lower than that of 3D-Cu; this may be a result of the Ag-activated Li nucleation kinetics.
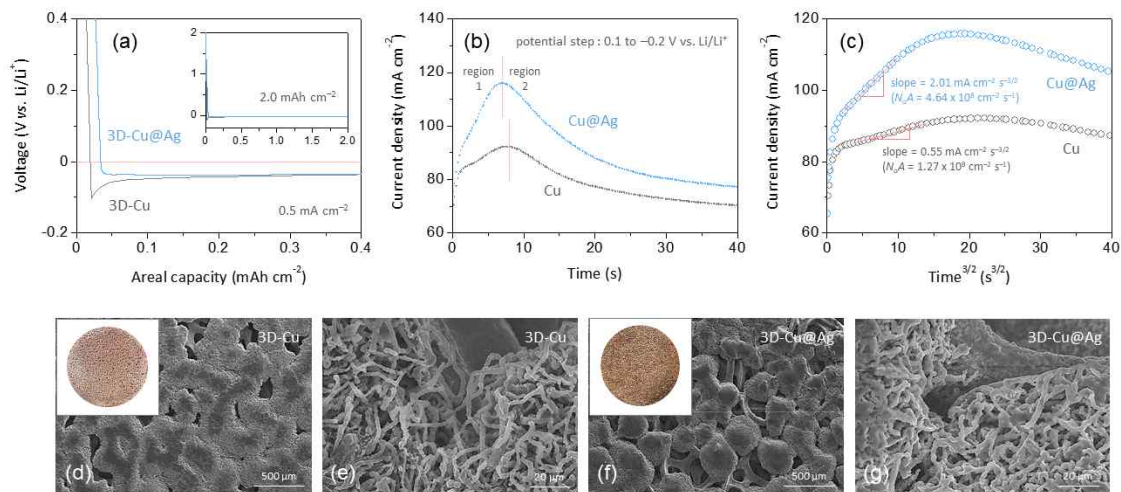
Figure 9. (a) Voltage profiles of 3D-Cu and 3D-Cu@Ag architectures measured during Li plating (2 mA h cm^{-2} at 0.5 mA cm^{-2}). (b) Current transients (current density (*i*) *vs.* time (*t*)) for Cu and Cu@Ag obtained by applying a cathodic potential step form 0.1 to-0.2 v *vs.* Li/Li^{+}. (c) Plots of *i* *vs.* t$^{3/2}$ reproduced from (b). SEM images of (d and e) 3D-Cu and (f and g) 3D-Cu@Ag taken after Li plating (2 mA h cm^{-2} at 0.5 mA cm^{-2}). The photographs of the electrodes were also included in the insets of (d) and (f) [21].
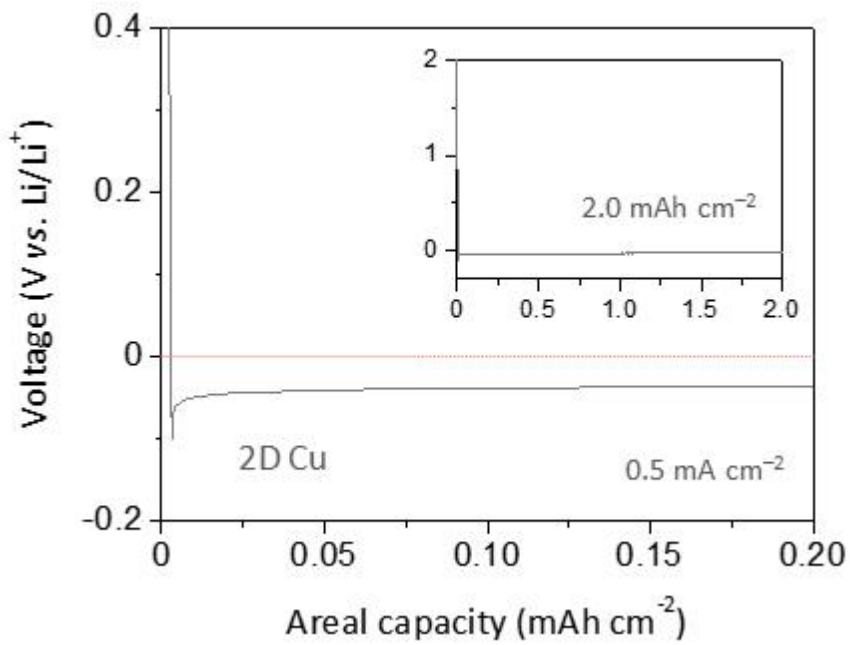
Figure 10. Voltage profile of the 2D Cu foil measured during Li plating (2 mA h cm^{-2} at 0.5 mA cm^{-2}) [21].

3. Top surface passivation and Li plating behavior of 3D-Cu@Ag │ AO architectures

The "top plating" phenomenon was observed on 3D-Cu@Ag, although it was observed to occur less frequently than on 3D-Cu, which has been found to exhibit enhanced Li nucleation kinetics. To better understand the top plating phenomena and alleviate this issue, we conducted a theoretical simulation study on the Li plating process using a porous architecture (Figure 11). Figure 11(b) sshows the equivalent circuit used to model Li plating, composed of two sub-circuits, Z_s and Z_p, connected in parallel. Z_s and Z_p represent the Li plating reactions on the top surface (designated as '1' in Figure 11(a)) and within the porous architecture (designated as '2' in Figure 11(a)), of the 3D framework, respectively. For simplicity, we assumed finite-length Li$^+$ migration in a cylindrical pore with an impermeable boundary at the end of the pore, and modeled Z_p using a modified transmission line [44, 45]. The theoretical analysis of an equivalent circuit was conducted using a circuit simulator known as the simulation program with integrated circuit emphasis (SPICE) [46].

The electrochemical response during Li plating was computed by applying a constant current density of 0.5 mA cm^{-2} to the equivalent circuit of Figure 11(b)). The local current density was the highest on the top surface and decreased with increasing pore depth. This may be attributable to limited Li$^+$ transport in the electrolyte-filled pores. This means that preferential Li plating on top of the 3D architectures was unavoidable even if Li nucleation kinetics on the inner surface (pore wall) was easy; this is consistent with the experimental results (Figure 9(d) and (f)). In the presence of protrusions or edges on the surface, as was the case for Cu@Ag foam, the problem of top plating was more pronounced as the electric field distribution will be uneven and Li$^+$ flux concentration occurs on the tip or edges. Simulations were also conducted using a 100-fold lower $R_{ct,s}$ value to mimic the Li$^+$ flux on the top surface being suppressed, as shown in Figure 11(d). The results show that by reducing $R_{ct,s}$, the local current density of the Li plating inside the pores increases, and the decrease in top surface activity (passivation) results in a uniform Li$^+$ flux to the porous structure. This suggests that may provide an effective approach to facilitate homogeneous Li$^+$ flux.
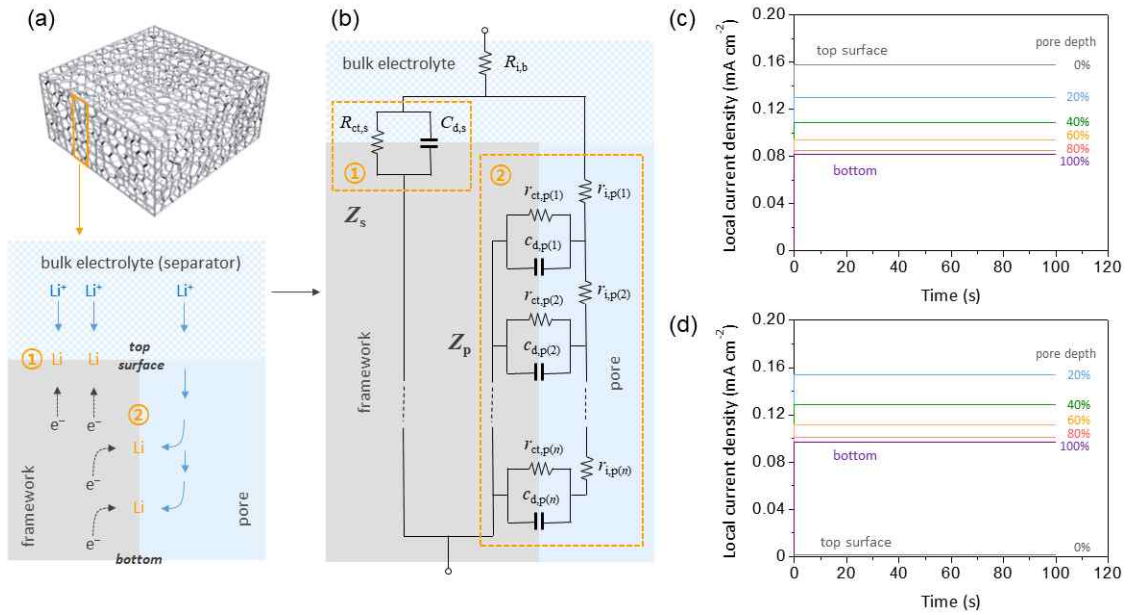
Figure 11. Schematic diagram for the Li plating process in a porous architecture. The reactions dem=noted as 1 and 2 represent Li plating on the top surface and inside the porous structure, respectively. (b) Equivalent circuit used to model the Li plating process illustrated in (a). Z_s and Z_p indicate the sub-circuites for reactions 1 and 2, respectively. R and C represent the resistance and capacitance, respectively, while r and c are the resistance and capacitance per unit length (thickness), respectively. The subscipt 'i' stands for the ionic conduction, 'ct' the charge transfer, 'd' the doublelayer charging, 'b' the bulk electrolyte, 's' the top surface, and 'p' for pore. Local current densities on different locations of the 3D architecture calculated using (c) $R_{ct,s}$ = 25.7 Ω cm^2 and (d) $R_{ct,s}$ = 2570 Ω cm^2. the total current density was 0.5 mA cm^{-2} [21].

4. Cell performance

Based on , the top surface of 3D-Cu@Ag was passivated by an AO coating to alleviate top surface plating and achieve uniform Li plating. Figure 12(a) shows the surface SEM imagery of 3D-Cu@Ag|AO and the corresponding EDS mapping results for Al. These results confirmed the presence of a uniform and dense Al_2O_3 coating on the top surface. Figure. 12(b) shows a typical voltage profile of 3D-Cu@Ag|AO measured upon Li plating (2.0 mA h cm^{-2} at 0.5 mA cm^{-2}). Similar to 3D-Cu @Ag, there were no features of the Li nucleation barrier observed, and the total overpotential was found to be approximately − 40 mV. Importantly, a significant difference was observed between the surface morphology of 3D-Cu@Ag and 3D-Cu@Ag|AO following Li plating. The photograph and SEM image in Figure 12(c), shows that no top plating of Li dendrites occurred on 3D-Cu@Ag|AO upon Li plating at 2.0 and 5.0 mA h cm^{-2} (Figure 13). Instead, spherical Li deposits were observed across the electrode surface (Figure 12(d) and (e)). In addition, high-magnification SEM imagery of the top and back surfaces taken after Li plating for 20 mA h cm^{-2} confirmed significant improvements in the uniformity of Li plating on 3D-Cu@Ag|AO (Figure 18) than on 3D-Cu (Figure. 18). This uniform Li plating may be attributed to the synergistic roles of (i) surface activation by the GD-Ag deposition, and (ii) surface passivation by the AO top-coating, uniform Li nucleation, and Li^+ transport, within the 3D architecture.

To assess the reversibility of the Li plating–stripping processes, the Coulombic efficiency (CE) was determined using a step-wise procedure (Figure 14) [47]. First, the electrode was plated with 2.0 mA h cm^{-2} of Li reservoir (denotedas '1' in Figure 14(a)), subjected to 10 cycles of Li plating and stripping with 1.0 mA h cm^{-2} (denotedas'2' in Figure 14(a)), and finally discharged to 1.5 V vs. Li/Li^+(denotedas'3' in Figure 14(a)).

CE measurements were conducted with a current density of 1.0 mA cm^{-2}. Prior to the CE experiment, electrodes were pre-conditioned by Li plating to 2.0 mA h cm^{-2} and subsequent Li stripping to 1.5 V vs. Li/Li^{+}. As expected, the average CEs were estimated to increase in the ascending order: 3D-Cu (92.9%), 3D-Cu@Ag (95.6%), and 3D-Cu@Ag|AO (98.2%). Figure 14(b) shows the cycling performances of the 3D architecture electrodes measured with 1.0 mA h cm^{-2} at 1.0 mA cm^{-2}. The Li ∥ 3D-Cu and Li ∥ 3D-Cu@Ag cells showed a dendrite-induced short circuit after ~83 cycles (~166 h) (Figure 14(c)) and ~105 cycles (~210 h) (Figure 14(d)). However, Li ∥ 3D-Cu@Ag|AO cell showed stable cycling operation for 125 cycles (~250 h) without any signs of damage due to dendrites (Figure 14(e)). It should be noted that 3D-Cu|AO without GD-derived Ag experienced a premature death after ~75 cycles (~150 h) (Figure 15, 16), demonstrating the efficacy of the combined surface activation–passivation technique.
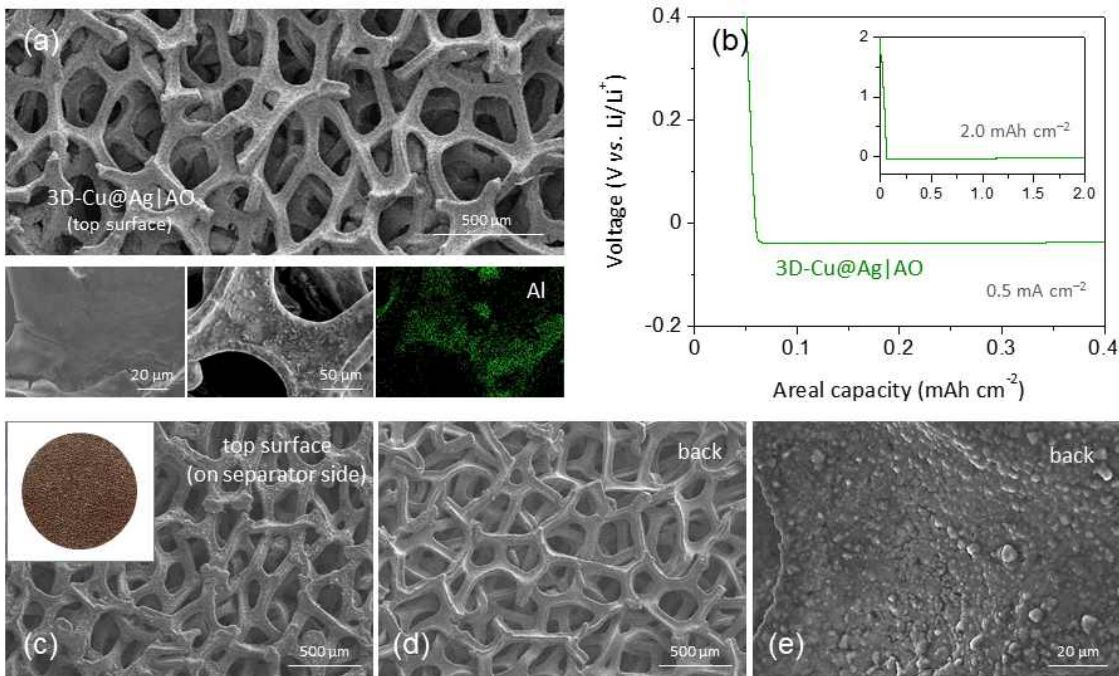
Figure 12. (a) SEM images and the corresponding EDS mapping result for Al obtained on a 3D-Cu@Ag|AO architecture. (b) Voltage profile of 3D-Cu@Ag|AO measured during Li plating (2 mA h cm^{-2} at 0.5 mA cm^{-2}). SEM images of 3D-Cu@Ag|AO taken after Li plating (2 mA h cm^{-2} at 0.5 mA cm^{-2}): (c) top surface facing the separator) and (d and e) back side. The photograph of the electride was also included in the inset of (c) [21].

2D Cu   2D Cu@Ag
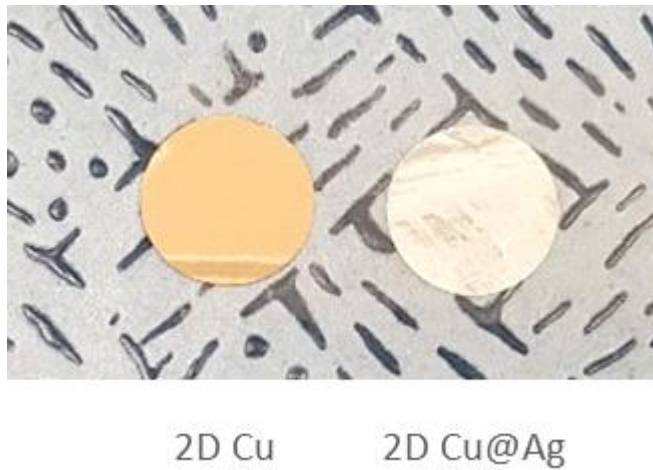
Figure 13. Photographs of 2D Cu and Cu@Ag foils. The 2D Cu@Ag foil was prepared by the GD process for t_{GD} = 10 s [21].
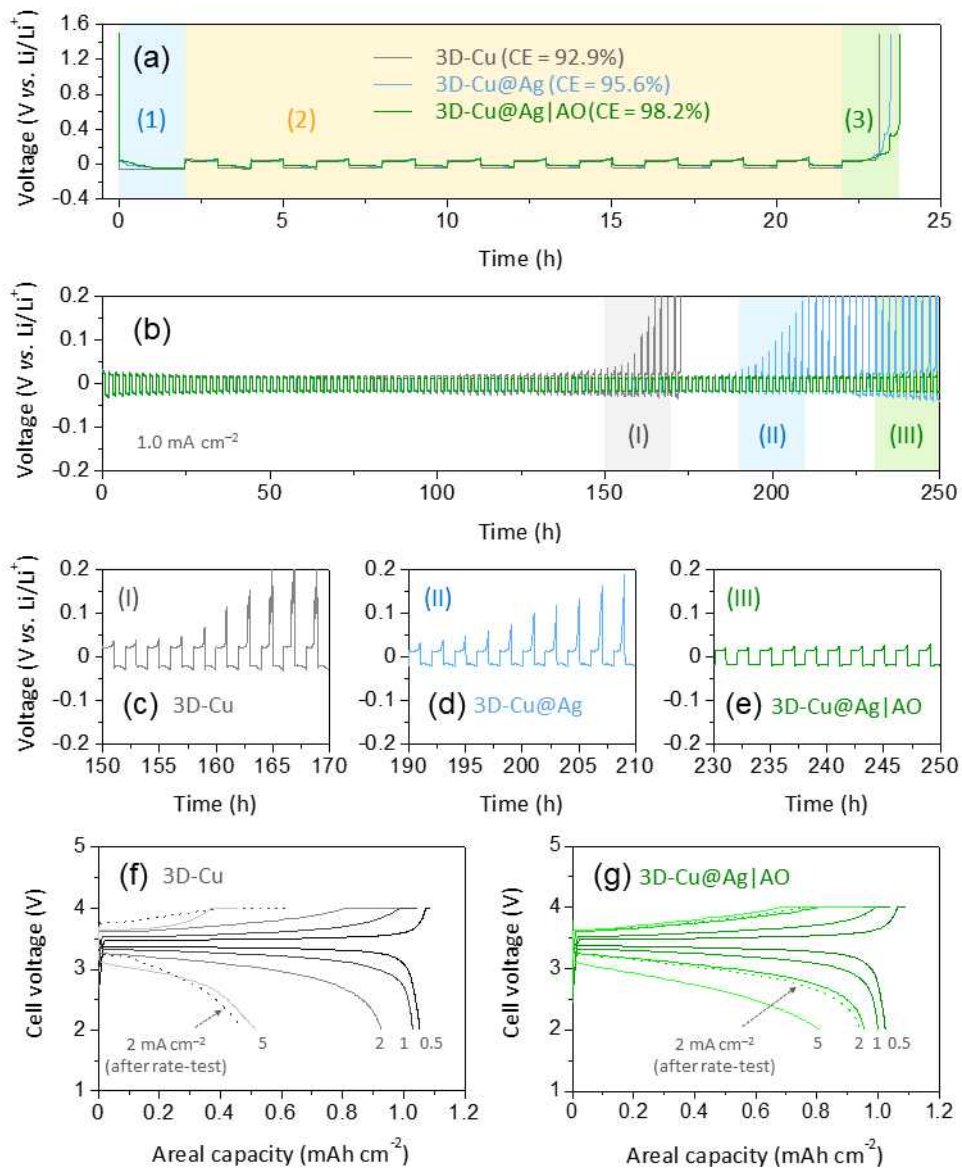
Figure 14. (a) Estimation of CEs and (b-e) cycling performance for 3D-Cu, 3D-Cu@Ag, and 3D-Cu@Ag|AO. Step 1, 2 and 3 in (a) represent the Li reservoir plating, Li plating-stripping cycling, and full Li stripping, respectively. The measurements were conducted at 1.0 mA cm^{-2}. Charge-discharge profiles of full cells with (f) 3D-Cu and (g) 3D-Cu@Ag|AO anodes. The cells were constructed using a LiFePO$_4$ cathode. The areal capacity of the cathode was ~1 mA h cm^{-2} [21].
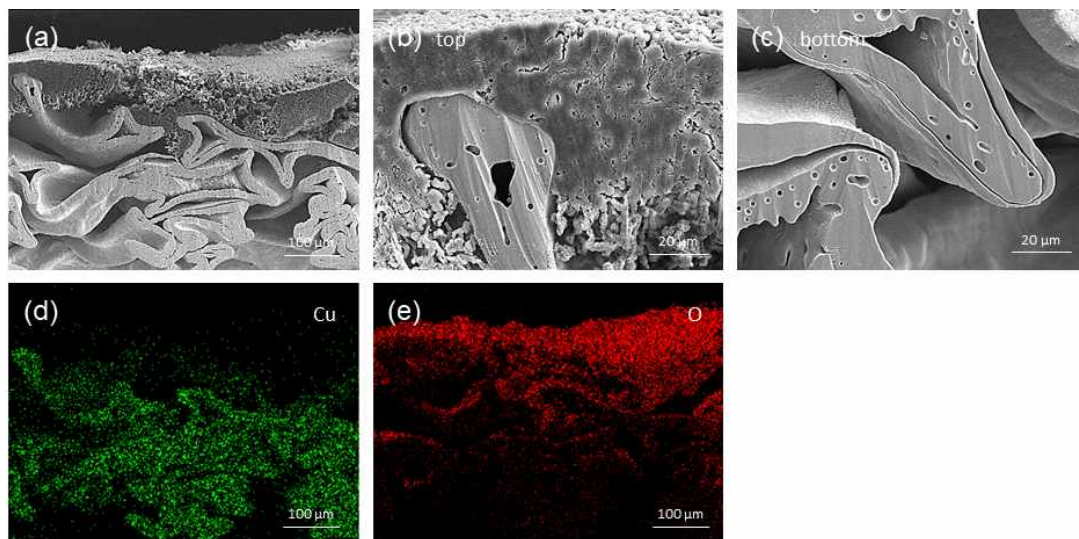
Figure 15. (a-c) Cross-sectional SEM images of 3D-Cu taken after Li plating (2 mA h cm^{-2} at 0.5 mA cm^{-2}) and (d,e) the corresponding EDS mapping results for Cu and O. The electrode was exposed to ambient atmosphere prior to EDS analysis, and the oxygen signal was recorded to determine the spatial distribution of LiO_x [21].
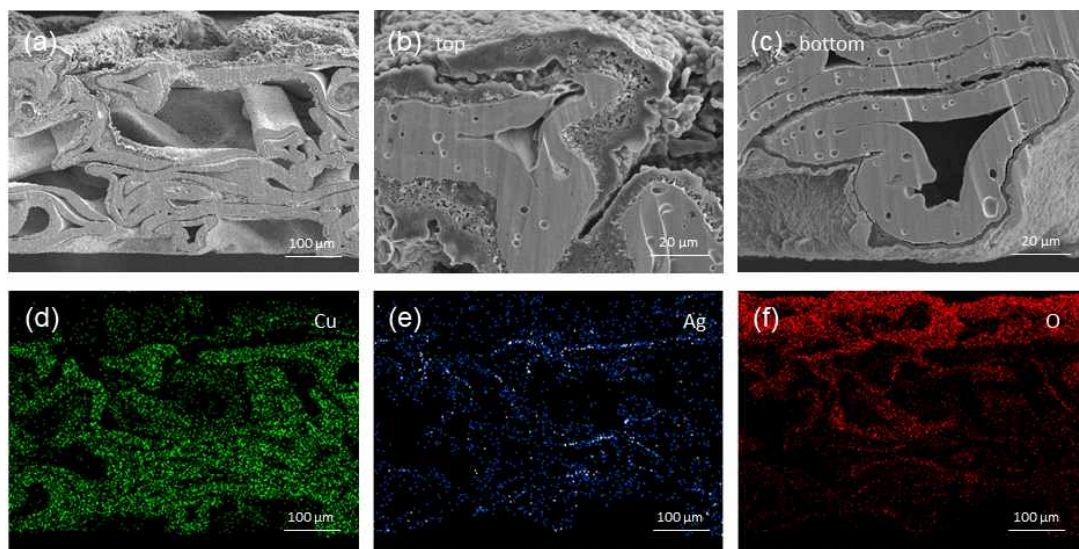
Figure 16. (a-c) Cross-sectional SEM images of 3D-Cu@Ag taken after Li plating (2 mA h cm^{-2} at 0.5 mA cm^{-2}) and (d-f) the corresponding EDS mapping results for Cu, Ag and O. The electrode was exposed to ambient atmosphere prior to EDS analysis, and the oxygen signal was recorded to determine the spatial distribution of LiO_x [21].
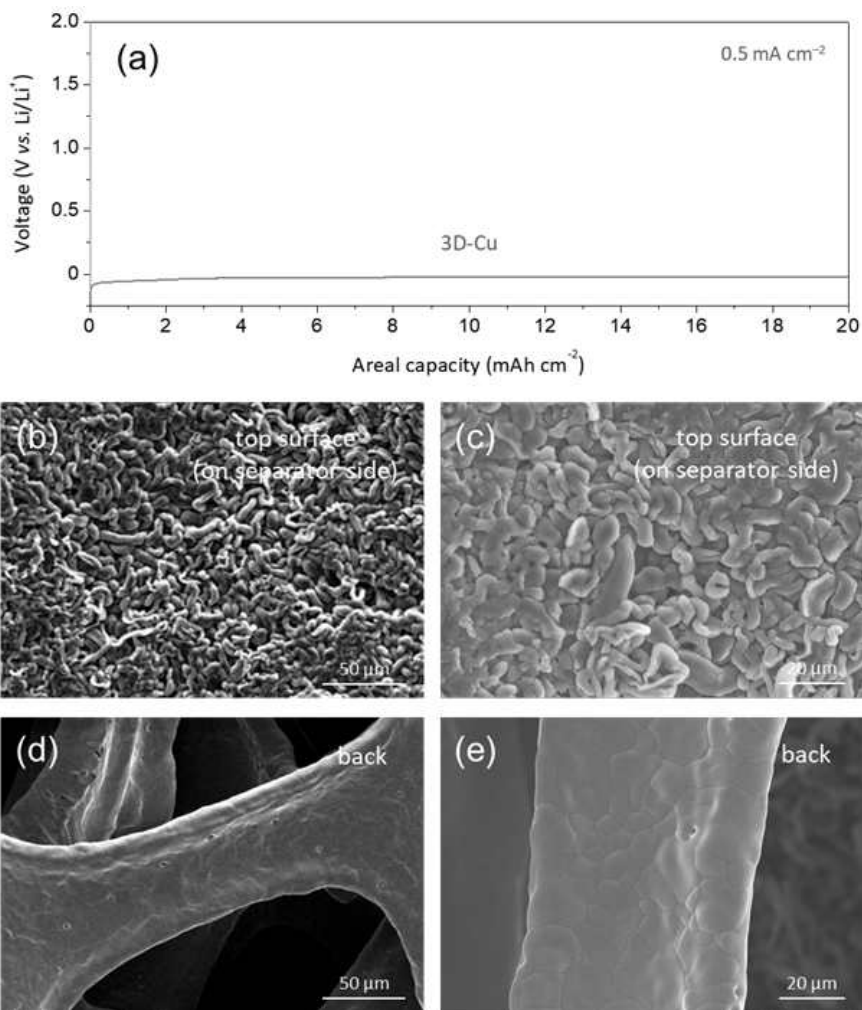
Figure 17. (a) Voltage profile of 3D-Cu measured during Li plating (20 mA h cm^{-2} at 0.5 mA cm^{-2}) and (b-e) SEM images taken after Li plating: (b, c) top surface (facing the separator) and (d, e) back side. Note that Li deposits were only observed on the top surface [21].
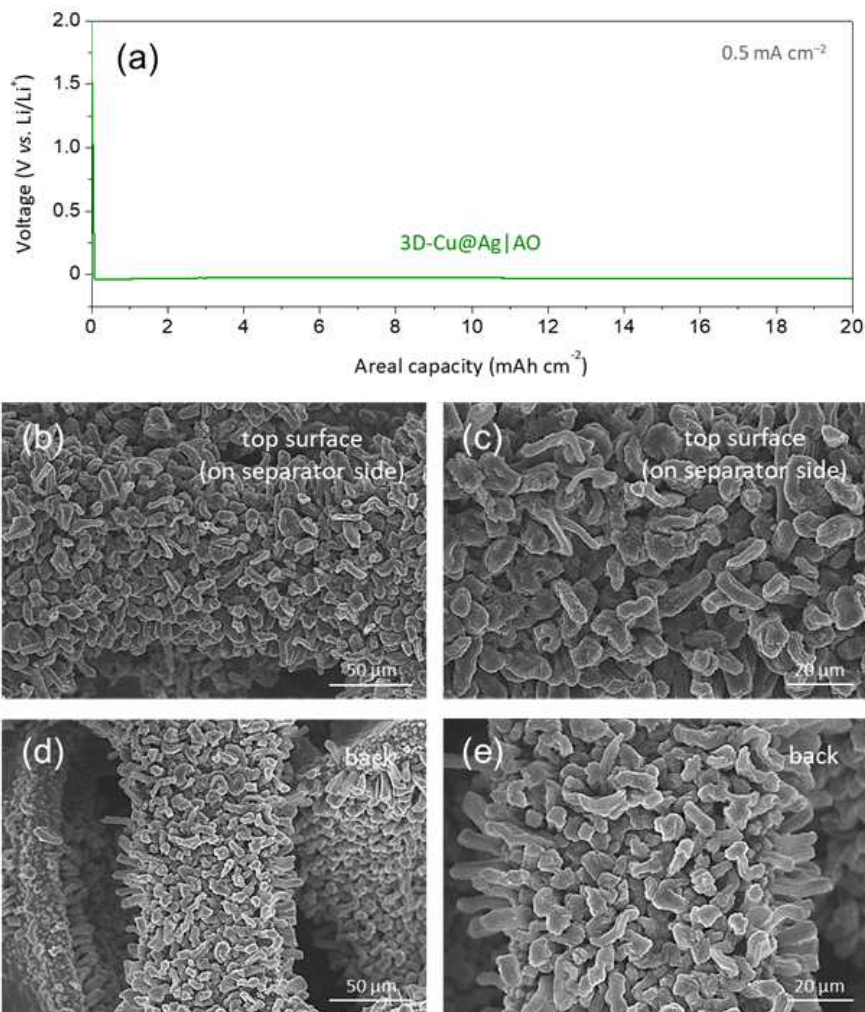
Figure 18. (a) Voltage profile of 3D-Cu@Ag|AO measured during Li plating (20 mA h cm^{-2} at 0.5 mA cm^{-2}) and (b-e) SEM images taken after Li plating: (b, c) top surface (facing the separator) and (d, e) back side. Note that Li deposits were only observed on the top surface [21].

Ⅳ. Interfacial activity gradient on porous architecture

A. Experimental methods

1. Materials synthesis

For Ag-deposited Cu mesh (or foil), a commercially available Cu mesh (wire diameter = 50 μm and spacing between wires = 77 μm), or foil (thickness = 20 μm) was washed with deionized water and subsequently with ethanol to remove residual impurities. A uniform and conformal Ag layer was formed on the Cu mesh via the GD process. The solution for GD was prepared by dissolving 59 mM $AgNO_3$(99.9%,Samchun), 0.58 M $(NH_4)_2SO_4$(99.0%, Samchun), and 3.78 M NH_4OH (28% NH_3 In H_2O, Sigma-Aldrich) in distilled water, followed by purging with N_2 gas. Following immersion of the Cu mesh in the prepared solution for 10 s, the Ag-deposited mesh was rinsed again with deionized water and ethanol and dried in a vacuum for 24 h. For the PVdF-coated Cu mesh, PVdF (5 wt.%) was fully dissolved in NMP over 24 h. The Cu mesh was immersed in the prepared PVdF solution, and the resulting specimen was dried at room temperature for 24 h. The 3D framework electrode was fabricated by stacking the selected meshes.

2. Materials characterizations

The microstructure and surface chemistry of samples were investigated using SEM (Hitachi S-4800) coupled with EDS. For post-test SEM characterization, samples were cleaned with 1, 2-dimethoxyethane (DME, Sigma-Aldrich) to remove residual substances. The crystal structure and phase were characterized using an automated Rigaku X-ray diffractometer (2500 D/MAX, Rigaku) using Cu $K\alpha$ (λ = 1.5405 Å) radiation.

3. Electrochemical experiments

Coin cells (CR-2032) were prepared using the fabricated frameworks as (working) electrodes, polypropylene separators (Celgard 3501), and electrolytes of 1 M lithium bis(trifluoromethanesulfonyl)imide (LiTFSI) in dioxolane (DOL)/DME (1:1 by volume) with 1 wt.% $LiNO_3$. The cell set up was completed by using Li-metal foil (diameter=0.6cm) as the counter electrode. Li plating was carried out at a fixed current density of 0.5 mA cm^{-2} for various capacities ranging from 5 to 40 mA h cm^{-2}. The reversibility of Li plating and stripping was examined through galvanostatic cycling at a constant current density of 0.5 mA cm^{-2} in two different ways: (i) Li plating (charging) for 1 mA h cm^{-2} and stripping (discharging) until 1.5 V vs. Li/Li$^+$; and (ii) Li plating and stripping at a fixed capacity of 1 mA h cm^{-2}. The electrochemical measurements were conducted at 25 ℃ using a battery tester (WonATech, WBCS3000S). To determine the electrical parameters utilized in theoretical modeling, electrochemical impedance spectroscopy was conducted with a Bio-Logic SP-200 electrochemical workstation using a 5 mV alternating current (AC) signal in a frequency range of 1 to 5 mHz.

B. Result and discussion

1. 3D porous architecture with interfacial activity gradient

Figure 19 is a schematic of the Li plating phenomena in the 3D framework electrodes during charging. The Li plating process in a porous architecture involved three key reactions that compete with each other (Figure 19(a)): (i) Li^+ migration toward the bottom (facing the current collector) in electrolyte-filled pores; (ii) (facing the separator); and (iii) interfacial charge-transfer (Li^+ reduction) on the surface of the architecture [21, 48, 49]. In general, Li^+ transport within the electrolyte-filled pores is relatively slow and imposes high ionic resistance. However, electron conduction through metal frameworks with uniform and rational surface activity (e.g., 3D-Cu), Li nucleation and subsequent growth preferentially occur on top of the electrode, leaving internal pores empty (Figure 19(b)). During continuous cycling, the top plating process may cause uncontrollable and non-uniform dendritic growth of Li, resulting in significant performance degradation and safety issues (internal short-circuiting). Given the competition between Li^+ transport and interfacial Li^+ reduction, the Li plating process may be directed to the bottom through proper . It is necessary to reduce the surface activity of the top region, suppress the reduction of Li^+ in this region and concurrently move Li^+ deeper into the architecture, although the interfacial reaction must be promoted in the bottom region. Therefore, Li accumulated and grew from the bottom of the electrode, gradually filling the voids (Figure 19(c)). The plated Li species would be confined in the 3D framework electrode, enabling stable long-term cycling.

To demonstrate the manipulation of the Li plating pattern via interfacial activity tuning, we fabricated a "model" architecture for the 3D architecture electrode by stacking Cu wire networks (meshes) with well-defined geometries (wire diameter = 50 μm; spacing between wires = 77 μm). The photographs and SEM imagery of Cu meshes are shown in Figure 20. In a proof-of-concept study, the interfacial activity of Cu was adjusted using either lithiophilic Ag for activation or insulative PVdF for passivation. In particular, Ag was known to reduce the activation energy barrier for Li nucleation and improve the interfacial kinetics of Li plating [21, 35, 50]. A previous study [21] has reported that a nanoscale Ag layer (thickness ~400 nm) was formed on the Cu architecture surface via the GD of Cu by Ag^{2+}, visibly whitening the Cu mesh and foil (Figure 20(c–f)). The XRD patterns of the Ag-deposited Cu mesh showed no signs of the secondary phase and were in good agreement with the diffraction peaks of Ag and Cu (Figure 20(f)). In contrast, a PVdF film formed on the mesh surface via dip-coating, and the color of the coated test piece did not change (Figure 20). The amount of PVdF in the coating solution was controlled to be ~5 wt.% to prevent morphological changes in the Cu mesh at higher PVdF loadings. Note that the morphologies of bare Cu, Ag-deposited Cu (Cu@Ag), and PVdF-deposited Cu (Cu@PVdF) were observed to be similar, characterized by no pore-blocking that adversely impacted on Li^+ transport. The interfacial activities of the surface-modified Cu samples were characterized by AC-impedance spectroscopy (Figure 21), revealing that deposited Ag and PVdF effectively increased and reduced exchange current densities for Li plating, respectively, in comparison to bare Cu.
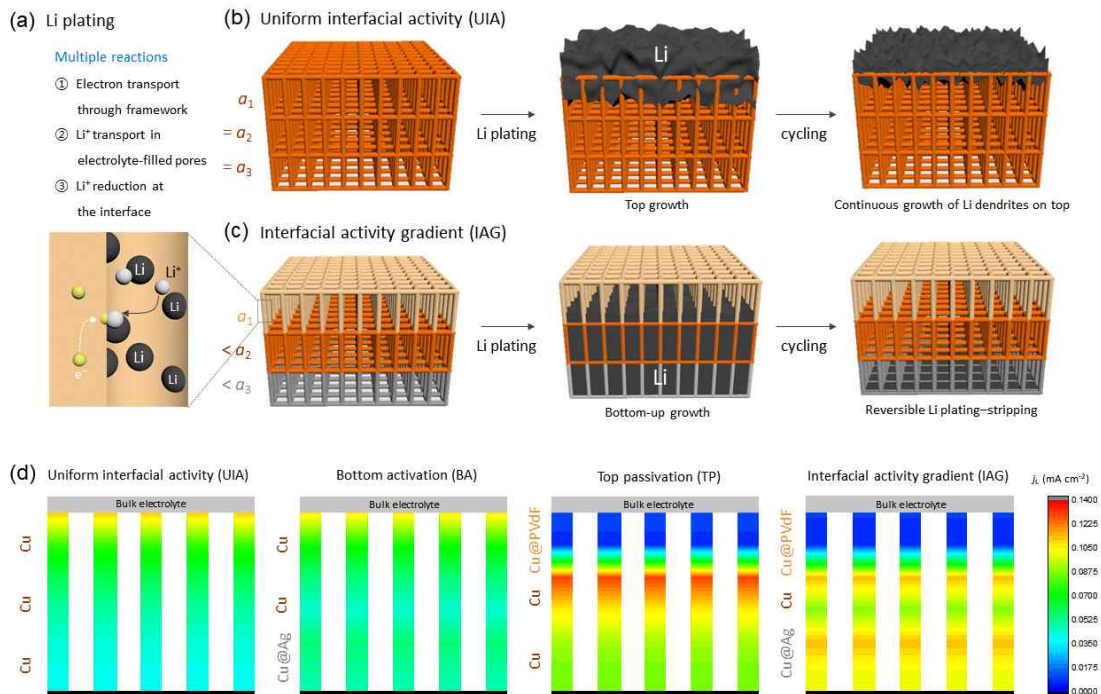
Figure 19. (a) Schematic illustration of the Li plating process in a 3D porous framework electrode. Li plating behaviors of 3D architecture electrodes with (b) uniform interfacial activity (UIA) and interfacial activity gradient (IAG). (d) Distribution maps of j_L in various architecture electrodes calculated at 0.5 mA cm^{-2} [22].
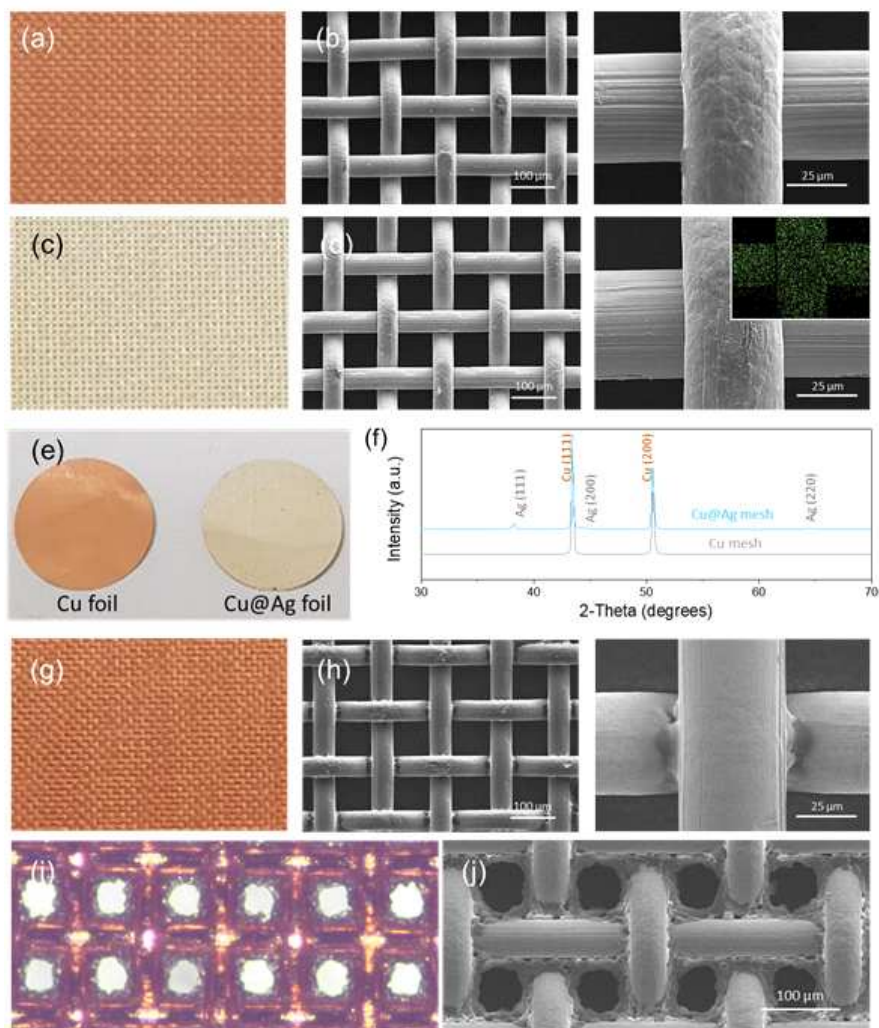
Figure 20. (a) Photograph and (b) surface SEM images of the bare Cu mesh. (c) Photograph and (c) surface SEM images and EDS silver distribution map of the Cu@Ag mesh. (e) Photograph of Cu and Cu@Ag foils. (f) XRD patterns of Cu and Cu@Ag meshes. (g, I) Phtograph and (h, j) surface SEM images of the Cu@PBdF meshes prepared using different PVdF solutions: (g, h) 5 wt% PVdF in NMP and (i, g) 10 wt% PVdF in NMP. The amount of PVdF in the coating solution was controlled to be ~5 wt% to prevent the morphological changes of the Cu mesh at higher PVdF loadings [22].
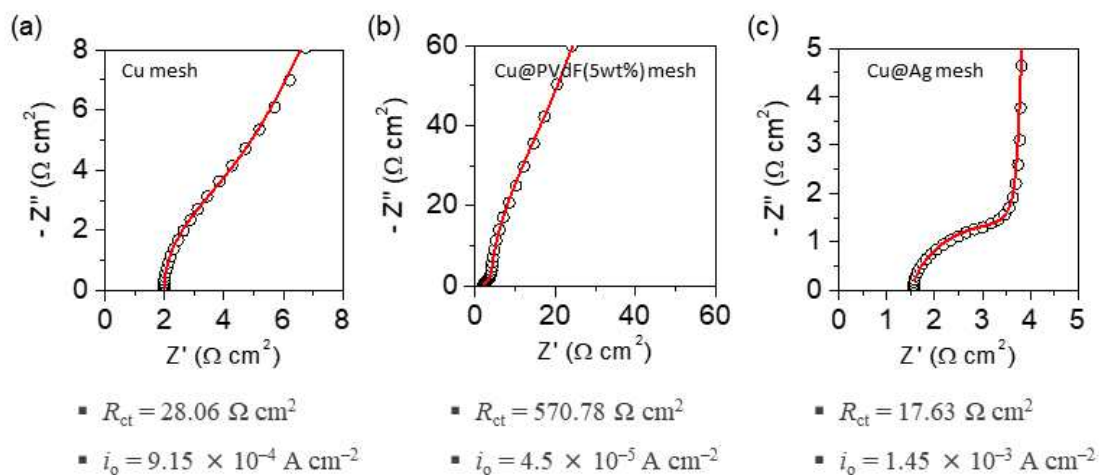
Figure 21. Nyquist plots of the AC-impedance spectra for various Cu meshes: (a) bare Cu, (b) Cu@PVdF, and (c) Cu@Ag. The open circles and lines indicate the measured and fitted data, respectively [22].

2. Theoretical simulations based on a transmission line model

The effect of interfacial activity tuning on Li plating behavior in the 3D architecture electrode was investigated by theoretical simulations based on a modified transmission line model (Figure. 22). The electrical parameters for simulation was determined from the AC-impedance results (Figure 21), electrolyte conductivity, and mesh geometries. Simulations were conducted on four different 3D framework electrodes using the circuit simulator, SPICE:

(i) *Uniform interfacial activity (UIA)*: [Cu | Cu | Cu] on Cu foil

(ii) *Bottom activation (BA)*: [Cu | Cu | Cu@Ag] on Cu@Ag foil

(iii) *Top passivation (TP)*: [Cu@PVdF | Cu | Cu] on Cu foil

(iv) *Interfacial activity gradient (IAG)*: [Cu@PVdF | Cu | Cu@Ag] on Cu@Ag foil

Figure 19(d) shows the distribution maps of local current densities (jL) for Li plating within the four types of framework electrodes calculated with an apparent current density of 0.5 mA cm^{-2} (see Figure 23 for the j_L *vs.* time curves at different pore depths). Using a conventional -Cu electrode, the value of jL rapidly drops with increasing pore depth when beginning at the top surface; this is indicative of top growth. This result may be attributed to the kinetic limitations of Li$^+$ transport within electrolyte-filled pores, preventing Li$^+$ from migrating deep inside. However, the jL distribution was modified by bottom activation (BA-Cu) or top passivation (TP-Cu); a relatively high jL value was predicted in the middle region. These results indicate that Li$^+$ transport may be further extended within the architecture by activating the bottom region with the lithiophilic phase or suppressing the interfacial activity of the top region with the insulating phase. Interestingly, the synergistic effect of both enables the IAG design to effectively adjust multiple reaction dynamics such that jL is concentrated in the bottom region (Figure 24(d)). This represents the advantages of IAG in terms of driving the bottom-up growth of Li.
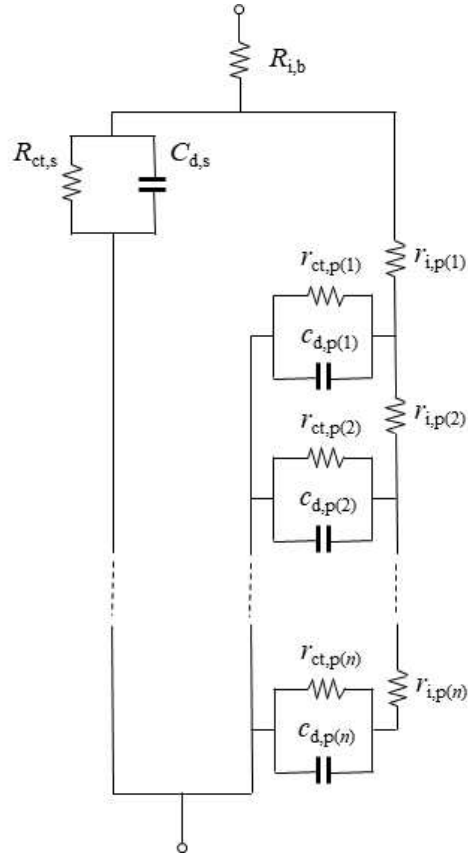
Figure 22. Equivalent circuit used to model the Li plating process. R and C represent the reisistance and capacitance, repectively, while r and c are the resistance and capacitance per unit length (thickness), respectively. The subscript 'i; stands for the ionic conduction, 'ct' the charge-transfer, 'd' the double-layer charging, 'b' the culk electrolyte, 's' the top surface, and 'p' for pore. The electricla parameters for the simulation were determined from the AC-impedance results (Figure 21), electrolyte conductivity, and mesh geometries [22].
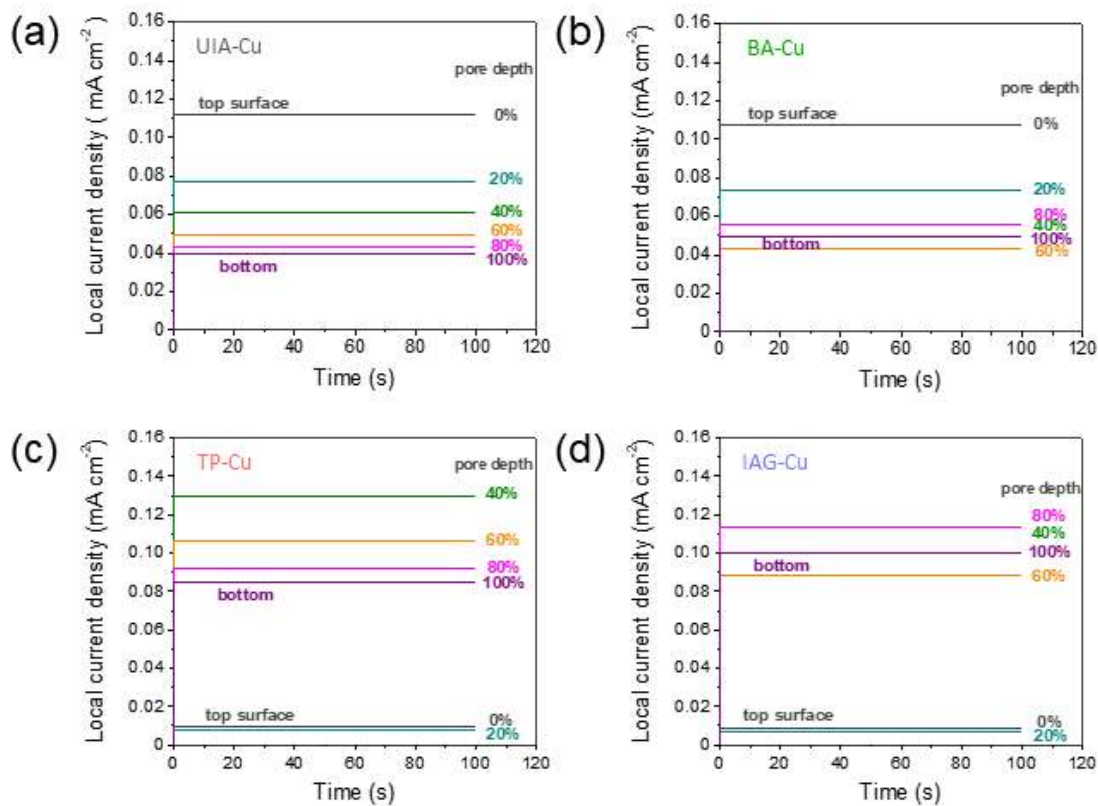
Figure 23. Local current densities (j_L) for Li plating in various architecture electrodes calculated at an apparent current density of 0.5 mA cm^{-2} [22].

3. Experimental study of the 3D architecture electrode

To validate these simulation results, we conducted a comparative experimental study of the architecture electrodes for Li plating with a fixed areal capacity of 5 mA h cm^{-2} at 0.5 mA cm^{-2}. The resulting voltage profiles of UIA-Cu and IAG-Cu, along with the SEM micrographs, are shown in Figure. 24, respectively. The voltage of UIA-Cu dropped to − 100 mV vs. Li/Li+ within a few minutes, then slightly increased, and finally remained constant at −70 mV vs. Li/Li$^+$ (Figure 24(a)). After plating, remarkable whitening was observed, indicating that Li was deposited on top of the electrode (inset of Figure 24(a)). Figure 24(b−j) shows the post-test SEM imagery and the results of EDS; these characterizations confirmed that the top region was completely covered with Li species (as detected by the O signal from oxidized Li species) (Figure 24(b−d)), However, the middle and bottom regions, did not contain Li (Figure 24(e−j) and 25). This is in good agreement with the simulation results shown in Figure 19(d). The BA-Cu and TP-Cu electrodes showed improvement in Li plating uniformity compared to UIA-Cu, respectively. The top plating observed on TP-Cu had Li$^+$ flux concentrated on the top surface due to the uneven morphology of entangled wires. The voltage of IAG-Cu slowly reached approximately −50 mV vs. Li/Li$^+$, and then had stabilized (Figure 24a). Based on prior studies, a large voltage drop (spike) in the early stages may be considered an energy barrier for Li nucleation. For the Cu architecture electrodes where the bottom region was modified with Ag, the Li nucleation barrier was reduced by the high affinity of Ag with Li, forming an Li−Ag solid solution, and resulting in monotonous voltage attenuation with reduced overpotentials (Figure 24(b)) [35, 51]. Note that the top and middle regions of the IAG-Cu were almost free of Li and retained their original porous structures (Figure 24(f−h)), while the Ag surfaces of the bottom region were evenly covered with Li deposits (Figure 24(h−j) and 26).

The Li plating behavior of IAG-Cu was also investigated for higher areal capacities of 20, 30, and 40 mA h cm^{-2}; these results are shown in Figure 28. The voltages remained constant at approximately −25 mV vs. Li/Li+ without a large voltage spike occurring during the early stage. The post-test SEM analysis showed the formation of significant Li deposits in the bottom region at 20 mA h cm^{-2}, where these deposits gradually filled the void spaces with increasing capacity, providing evidence for the bottom-up growth pattern of Li. In comparison to IAG-Cu, UIA-Cu also showed significant top growth at 20 mA h cm^{-2} (Figure 27). This indicates that IAG engineering is an effective means of facilitating the bottom to outward Li plating and takes full advantage of the potential benefits of 3D architecture electrodes.
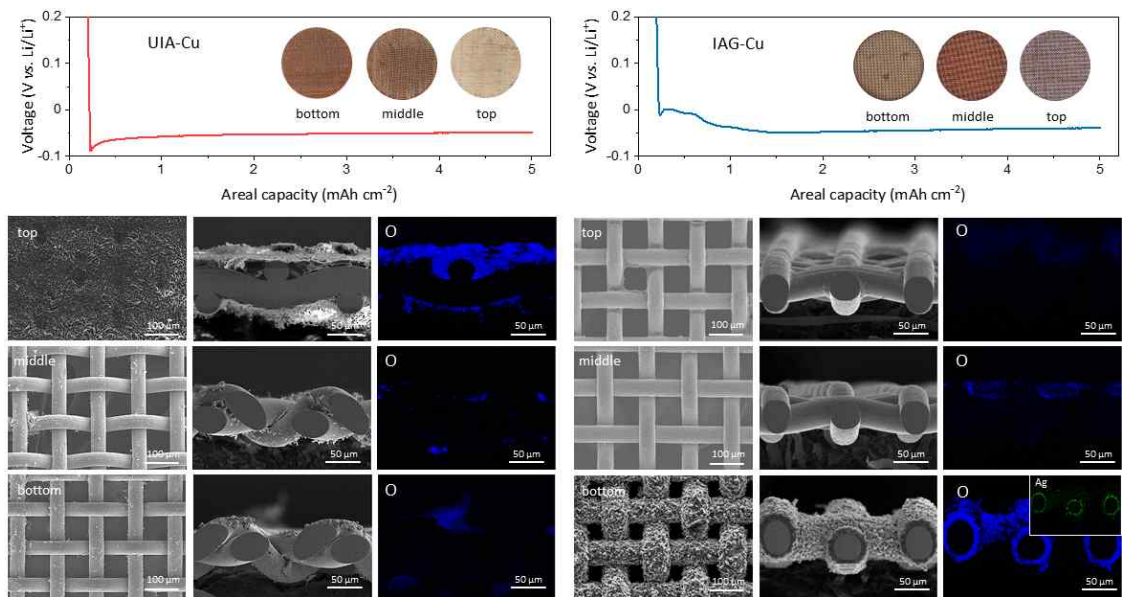
Figure 24. Voltage profiles of (a) UIA-Cu and (b) IAG-Cu measured during Li plating for 5 mAh cm^{-2} at 0.5 mA cm^{-2}. The photographs of the meshes collected after Li plating are presented. Surface and cross-sectional SEM images and EDS oxygen distribution maps of the meshes: (c-e) UIA-Cu and (f-h) IAG-Cu [22].
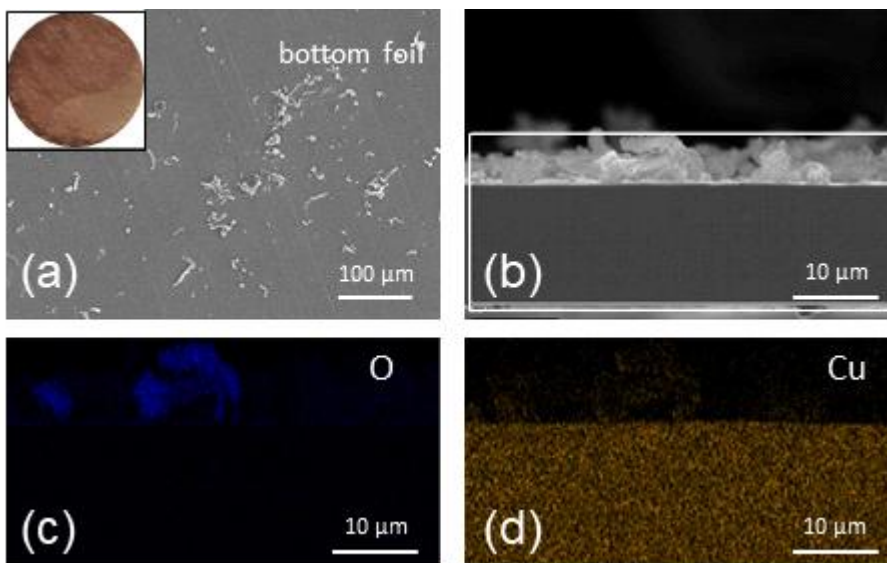
Figure 25. (a) Surface and (b) cross-sectional SEM images of the Cu foil used for UIA-Cu after Li plating. The photograph of the Cu foil is also presented in (a). (c, d) EDS oxygen and copper distribution maps for the region indicated in (b) [22].
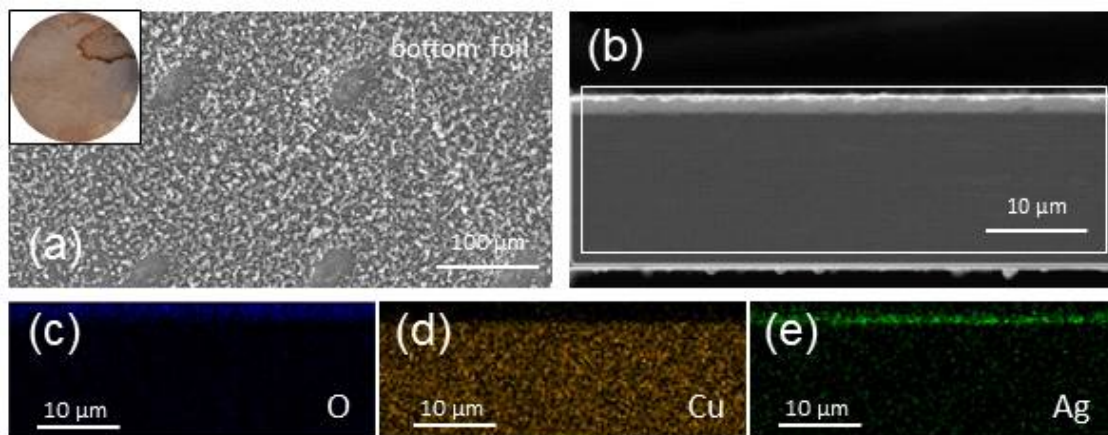
Figure 26. (a) Surface and (b) cross-sectional SEM images of the Cu@Ag foil used for IAG-Cu after Li plating. The photograph of the Cu@Ag foil is also presented in (a). (c-e) EDS oxygen, copper and silver distribution maps for the region indicated in (b) [22].
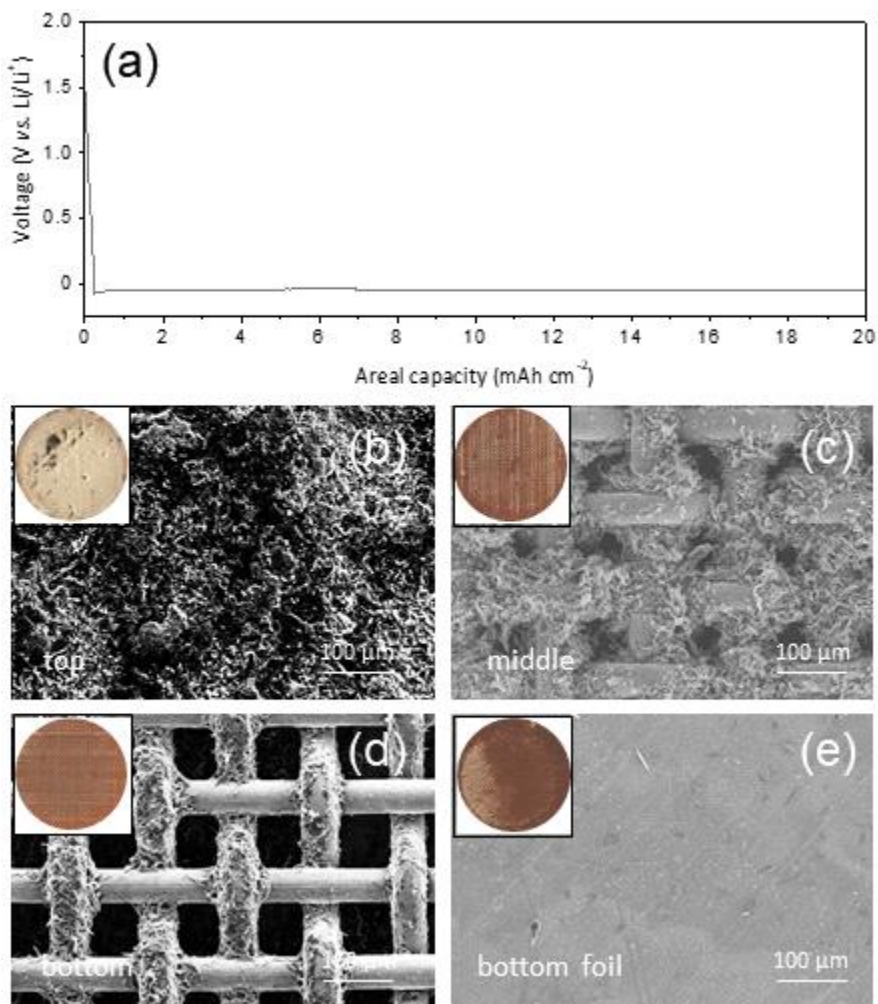
Figure 27. (a) Voltage profile of UIA-Cu measured during Li plating for 20 mA h cm^{-2} at 0.5 mA cm^{-2} and (b-e) surface SEM micrographe of the Cu meshes and foil obtained after Li plating. The photographs of the meshes collected after Li plating are also presented in (b-e) [22].

4. Cell performance

To evaluate the efficacy of interfacial activity tuning in improving the reversibility of Li plating and stripping, four types of Li ∥ 3D-Cu cells were subjected to galvanostatic cycling at a constant current density of 0.5 mA cm^{-2}, with Li plating for 1 mA h cm^{-2} and subsequent Li stripping to 1.5 V vs. Li/Li^{+}. Figure 28(h) presents the voltage profiles of cells assembled with UIA-Cu, BA-Cu, TP-Cu, and IAG-Cu electrodes, respectively. The BA-Cu and IAG-Cu electrodes exhibited stepped voltage behaviors during Li stripping, associated with the de-alloying of Li−Ag.

The CE was determined as the ratio of the stripping capacity to the plating capacity for each cycle, and its evolution with cycling is shown in Figure 29. The CE for all electrodes ranged from 60% to 75% in the early stage due to the formation of SEI, then increased rapidly as cycling proceeded. The UIA-Cu and TP-Cu electrodes maintained CEs at ~95% for 50 cycles, then it had decreased significantly to ~80% after ~115 and ~135 cycles, respectively. The BA-Cu electrode had a CE of ~96%, indicating the beneficial role of lithiophilic Ag in the bottom region. Importantly, the IAG-Cu electrode had a CE value as high as 98%, showing stable cycle performance over 200 cycles. In addition, Figure 28(h) compares the data from cycling experiments in which 5 mA h cm^{-2} of Li was pre-stored in the electrodes, and cells were cycled with a fixed areal capacity of 1 mA h cm^{-2} at 1 mA cm^{-2}. For Li plating, all the cells showed a constant voltages at approximately −50 mV vs. Li/Li^{+}. For the Li stripping process, the overpotential for IAG-Cu remained constant below 50 mV over 200 h (Figure 29),)), while the overpotential of other electrodes gradually increased and exceeded 200 mV in the descending order of UIA-Cu (~140 h, Figure 29(b)) > BA-Cu (~170 h, Figure 29(c)) ~ TP-Cu (~170 h, Figure 29(d)). The experimental results in Figure 28 and 29 show that the bottom-up growth behavior of Li was an essential prerequisite to improve the cycling stability of the 3D architecture electrodes.

This study demonstrated the use of a model architecture made of Cu wire networks to highlight the important role of interfacial tailoring in manipulating Li growth behavior. However, the effectiveness of IAG design may be improved further by controlling the microstructural factors of the 3D framework electrode, such as pore size, wall thickness, and electrode thickness. Figure. 30 shows a contour diagram of the uniformity (δ) in j_L for the UIA-Cu and IAG-Cu electrodes that was simulated to investigate the role of microstructural engineering in combination with interfacial activity tuning. Here, the parameter δ is defined as $\delta = (j_{L,t} - j_{L,b}) / j_{L,a}$, where $j_{L,t}$ and $j_{L,b}$ are the local current densities at the top and bottom, respectively; and $j_{L,a}$ represents the average current density (i.e., the applied current divided by the total microscopic area). Therefore, δ indicates different modes of Li growth; positive for top growth. and negative for bottom-up growth. The conventional UIA-Cu electrode had a positive δ value, regardless of the microstructural parameters, and showed dominant top growth behavior. This meant it was almost impossible to achieve uniform Li plating in UIA-Cu. the δ for the IAG-Cu electrode was predicted to be negative for any microstructural parameters, suggesting bottom-up growth. This type of growth may be promoted further by reducing the thickness of the electrodes and increasing the pore size or wall thickness. This improves the cycling stability of IAG-Cu compared to the model architecture that had been used. The simulations in Figure 30 provide fundamental insights into the structural design of 3D porous architectures for a robust and efficient Li electrode, and imply that electrode performance may be improved further by optimizing the porous framework structures and interfacial properties.
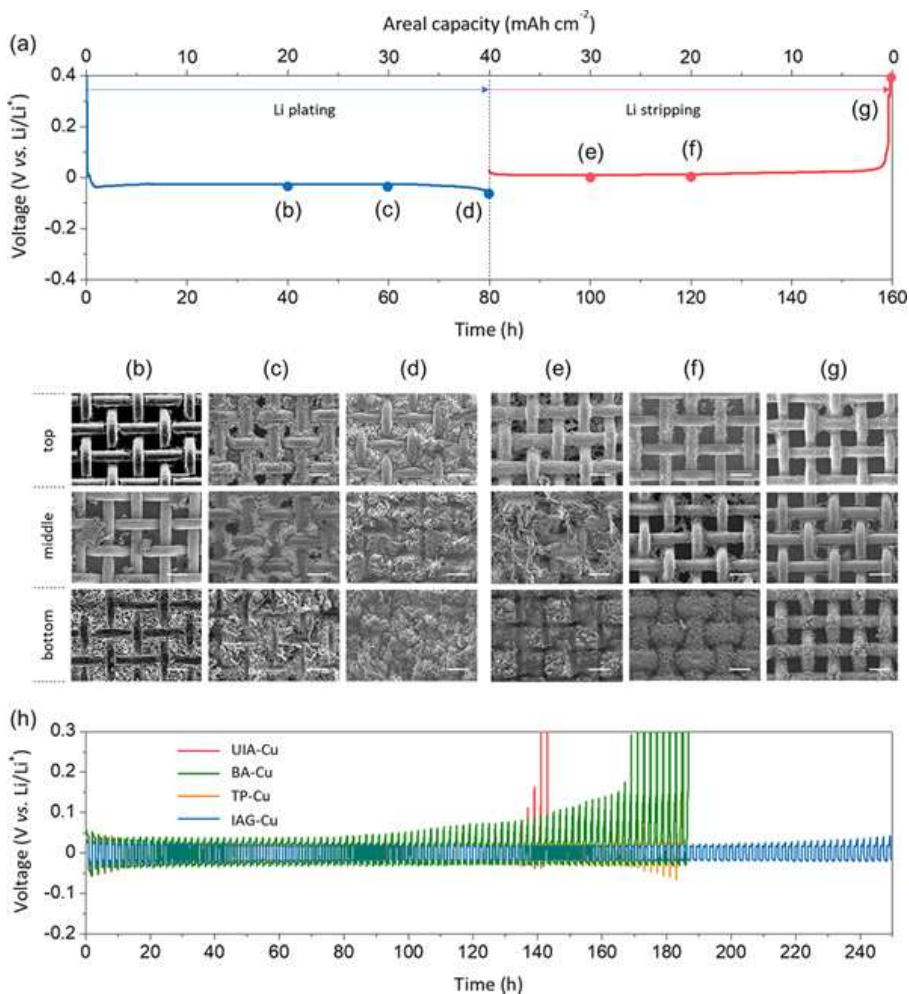
Figure 28. (a) Voltage profiles measured during Li plating-stripping at 0.5 mA cm^{-2} and (b-g) SEM micrographs at the selected capacity values. The scale bar indicates 100 μm. (h) Cycling performance during Li plating-stripping with a fixed capacity of 1 mA h cm^{-2} at 1 mA cm^{-2} [22].
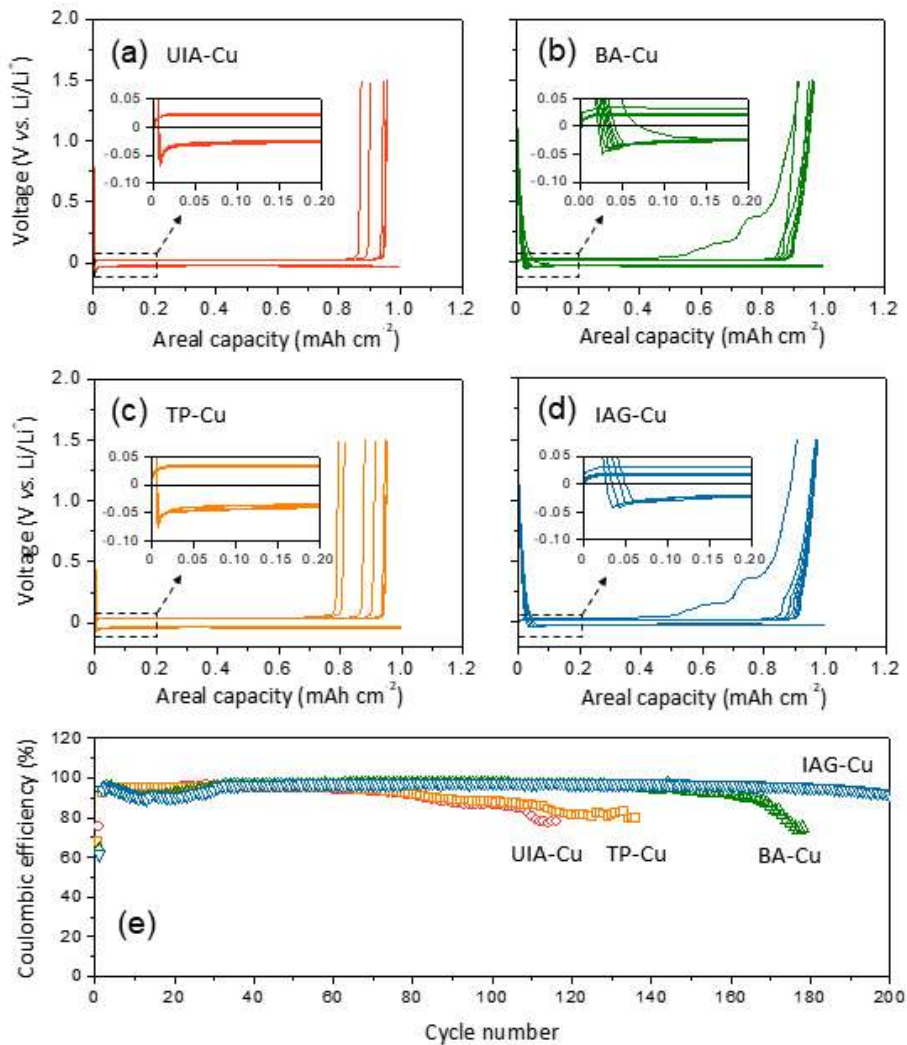
Figure 29. Voltage profiles of (a) UIA-Cu, (b) BA-Cu, (c) TP-Cu, and (d) IAG-Cu measured during Li plating-stripping cycling at 0.5 mA cm^{-2} and (e) the variation of CEs during cycling. Li was plated with an areal capacity of 1mA h cm^{-2}, and then Li was stripped until the voltage reached 1.5 V $vs.$ Li/Li^{+} [22].
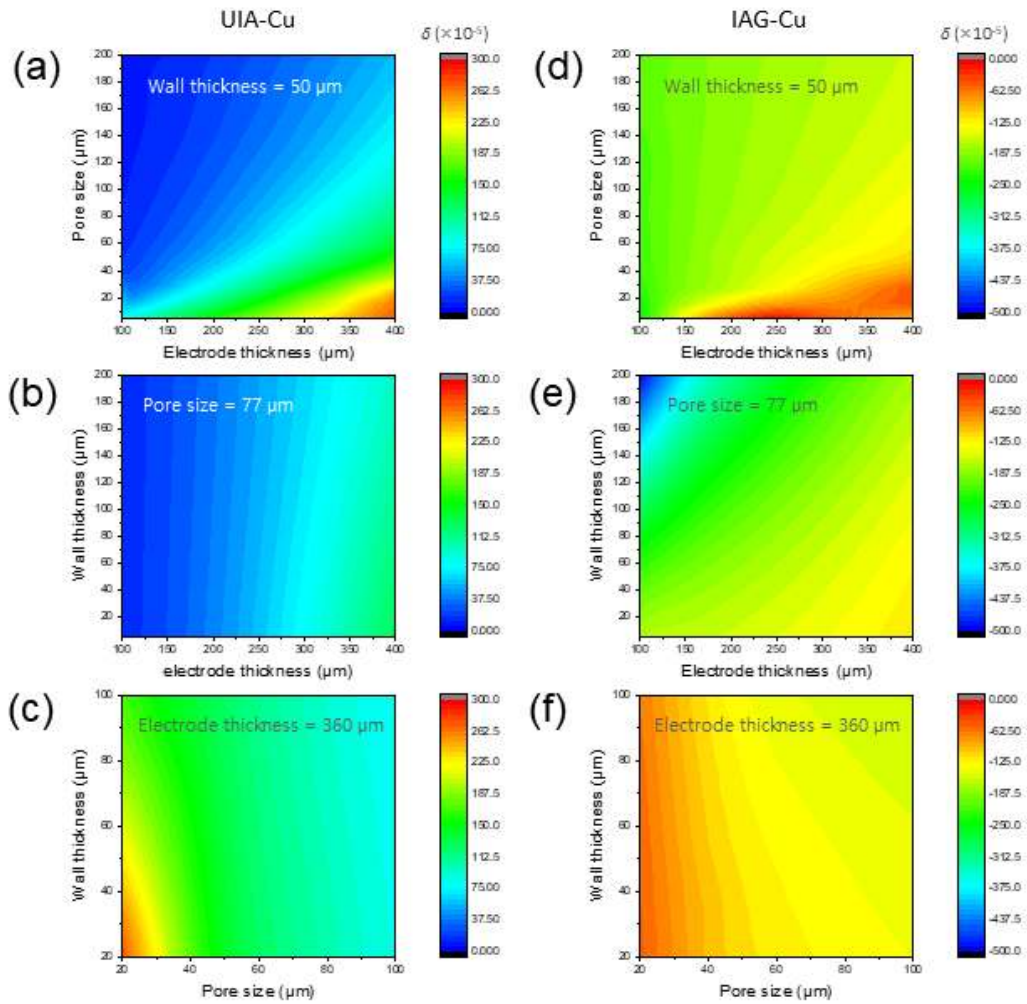
Figure 30. Contour plots of the uniformity (δ) in j_L for (a-c) UIA-Cu and (d-f) IAG-Cu simulated using various combinations of microstructural parameters [22].

Ⅴ. Conclusions

This study proposed a synergistic surface activation–passivation technique and a rational design of 3D architecture electrodes with an IAG. This was carried out to enable the bottom-up growth of metallic Li, enhancing the reversibility and cycling stability of Li. Theoretical simulations based on a modified transmission line model were conducted to predict the effect of interfacial activities on Li plating behavior. The surface activation and passivation of 3D-Cu was achieved by conformal deposition of a lithiophilic Ag nano-layer *via* GD and coating of inert Al_2O_3 on the top surface, respectively. Experimental studies and theoretical modeling showed that the Ag nano-layer reduced the energy barrier for Li nucleation, promoted uniform Li nucleation across the 3D-Cu surface, the Al_2O_3 coating provided homogeneous Li^+ flux into the porous architecture and inhibited undesirable top plating. Therefore, the synergistic role of surface conditioning, the 3D-Cu@Ag|AO electrode had a high CE of > 98% during Li plating and stripping with stable cycling behavior. This was achieved without optimization of the porous architecture, representing a significant improvement compared to the pristine 3D-Cu anode. The IAG design effectively adjusted multiple reaction dynamics to preferentially plate Li^+ on the bottom region while suppressing top growth. The bottom-up growth behavior of Li had been further substantiated by experimental studies using model architecture. The IAG-Cu framework electrode fabricated using lithiophilic Ag (in the bottom region) and insulative PVdF (in the top region) showed outstanding morphological stability during high-capacity Li storage (40 mA h cm^{-2}); the conventional Cu architecture was significantly top plating. Therefore, the IAG-Cu electrode exhibited an approximate two-fold improvement in cycling stability compared to the Cu electrode. This may be improved further by optimizing the porous architecture, as shown by the simulations. This study provides a guideline for the design and construction of 3D framework electrodes with a long cycle lifetime for rechargeable Li-metal batteries.

Ⅵ. References

1. j. b. Goodenough and K. -S. Park J. Am. Chem. SOC. 2013, 135, 1167-1176.

2. B. Liu, J.-G. Zhang, W. Xu. Joule 2018, 2, 833-845.

3. P. G. Bruce, S. A. Freunberger, L. J. Hardwick and J. M. Tarascon, Nat. Mater., 2012, 11, 19.

4. K.-N. Jung, J. Kim, Y. Yamauchi, M.-S. Park, J.-W. Lee and J. H. Kim, J. Mater. Chem. A, 2016, 4, 14050.

5. H. Zhao, N. Deng, J. Yan, W. Kang, J. Ju, Y. Ruan, X. Wang, X. Zhuang, Q. Li and B. Cheng, Chem. Eng. J., 2018, 347, 343.

6. S. Sripad, V. Viswanathan, ACS Energy Lett. 2017, 2, 1669－.1673.

7. W. L. Fredericks, S. Sripad, G. C. Bower, V. Viswanathan, ACS Energy Lett. 2018, 3, 2989－.2994.

8. V. Viswanathan, B. M. Knapp, Nat. Sustain. 2019, 2, 88－.89.

9. P. Bai, J. Li, F. R. Brushett and M. Z. Bazant, Energy Environ. Sci., 2016, 9, 3221.

10. K. N. Wood, M. Noked and N. P. Dasgupta, ACS Energy Lett., 2017, 2, 664.

8 S. Li, M. Jiang, Y. Xie, H. Xu, J. Jia and J. Li, Adv. Mater., 2018, 30, 1706375.

11. B. Liu, J.-G. Zhang and W. Xu, Joule, 2018, 2, 833.

12. D. Lin, Y. Liu, Y. Cui, Nat. Nanotechnol. 2017, 12, 194－.206.

13. H. Qiu, T. Tang, M. Asif, X. Huang, Y. Hou, Adv. Funct. Mater. 2019, 29, 1808468.

14. H. Liu, E. Wang, Q. Zhang, Y. Ren, X. Guo, L. Wang, G. Li, H. Yu, Energy Storage Mater. 2019, 17, 253－.259.

15. B. Hong, H. Fan, X.-B. Cheng, X. Yan, S. Hong, Q. Dong, C. Gao, Z. Zhang, Y. Lai, Q. Zhang, Energy Storage Mater. 2019, 16, 259－.266.

16. S. Chabi, C. Peng, D. Hu, Y. Zhu, Adv. Mater. 2014, 26, 2440－.2445.

17. Q. Li, S. Zhu, Y. Lu, Adv. Funct. Mater. 2017, 27, 1606422.

18. S.-S. Chi, Y. Liu, W.-L. Song, L.-Z. Fan, Q. Zhang, Adv. Funct. Mater. 2017, 27, 1700348.

19. Q. Yun, Y.-B. He, W. Lv, Y. Zhao, B. Li, F. Kang, Q.- H. Yang, Adv. Mater. 2016, 28, 6932－.6939.

20. J. Kim, J. Lee, J. Yun, S. H. Choi, S. A. Han, J. Moon, J. H. Kim, J.-W. Lee, M.-S.

Park, Adv. Funct. Mater. 2020, 30, 1910538.

21. J. Yun, E.-S. Won, H.-S. Shin, K.-N Jung, J.-W. Lee, J. Mater. Chem. A 2019, 7, 23208－.23215.

22. J. Yun, B.-K. Park, E.-S. Won, S. H. Choi, H. C. Kang, J. H. Kim, M.-S. Park, J.-W. Lee, ACS Energy Lett., 2020, 5, 3108-3114.

23. R. Zhang, N.-W. Li, X.-B. Cheng, Y.-X. Yin, Q. Zhang and Y.-G. Guo, Adv. Sci., 2017, 4, 1600445.

24. J. Liu, Z. Bao, Y. Cui, E. J. Dufek, J. B. Goodenough, P. Khalifah, Q. Li, B. Y. Liaw, P. Liu, A. Manthiram, Y. S. Meng, V. R. Subramanian, M. F. Toney, V. V. Viswanathan, M. S. Whittingham, J. Xiao, W. Xu, J. Yang, X.-Q. Yang and J.-G. Zhang, Nat. Energy, 2019, 4, 180.

25. C. Jin, W. Sheng, J. Luo, H. Yuan, C. Fang, W. Zhang, H. Huang, Y. Gan, Y. Xia, C. Liang, J. Zhang and X. Tafo, Nano Energy, 2017, 37, 177.

26. Y. Liu, D. Lin, Z. Liang, J. Zhao, K. Yan and Y. Cui, Nat. Commun., 2016, 7, 10992.

27. C. Yang, Y. Yao, S. He, H. Xie, E. Hitz and L. Hu, Adv. Mater., 2017, 29, 1702714.

28. D. Lin, Y. Liu, Y. Cui, Nat. Nanotechnol. 2017, 12, 194-206.

29. X.B. Cheng, R. Zhang, C.Z. Zhao, and Q. Zhang, Chem. Rev. 2017, 117, 10403－10473.

30. Y. S. Cohen, Y. Cohen, & D. Aurbach, J. Phys. Chem. B 104, 12282－12291 (2000).

31. H. Kim, G. Jeong, Y.-U. Kim, J.-H. Kim, C.-M. Park, and H.-J, Sohn, Chem. Soc. Rev., 2013. 42. 9011.

32. F. Orsini, A. D. Pasquier, B. Beaudoin, J. M. Tarascon, M. Trentin, N. Langenhuizen, D. E. Beer and P. Notten, J. Power Sources, 1998, 76, 19.

33. S. Chabi, C. Peng, D. Hu and Y. Zhu, Adv. Mater. 2014, 26, 2440-2445.

34. B. Hong, H. Fan, X.-B. Cheng, X. Yan, S. Hong, Q. Dong, C. Gao, Z. zhang, Y. Lai and Q. Dong, Energy Storage Materials, 2019, 16, 259-266.

35. K. Yan, Z. Lu, H.-W. Lee, F. Xiong, P.-C. Hsu, Y. Li, J. Zhao, S. Chu and Y. Cui, 2016, 1, 16010.

36. J. Yuan, Y. Lai, J. Duan, Q. Zhao and J. Zhan, J. Colloid Interface Sci., 2012, 365, 122.

37. H. Lee, S.-K. Kim and S. H. Ahn, J. Ind. Eng. Chem., 2017, 54, 218.

38. Z. Liu, N. Zhang, Z. Wang and K. Sun, J. Power Sources, 2012, 205, 479.

39. B. R. Schari er and J. Mostany, J. Electroanal. Chem., 1984, 177, 13.

40. M. E. Hyde, R. Jacobs and R. G. Compton, J. Phys. Chem. B, 2002, 106, 11075.

41. M. E. Hyde and R. G. Compton, J. Electroanal. Chem., 2003, 549, 1.

42. A. Pei, G. Zheng, F. Shi, Y. Li and Y. Cui, Nano Lett., 2017, 17, 1132.

43. P. Arora, M. Doyle and R. E. White, J. Electrochem. Soc., 1999, 146, 3543.

44. J. Jamnik and J. Maier, Phys. Chem. Chem. Phys., 2001, 3, 1668.

45. Z. Siroma, N. Fujiwara, S.-I. Yamazaki, M. Asahi, T. Nagai and T. Ioroi, Electrochim. Acta, 2015, 160, 313.

46. H.-M. Cho, Y. J. Park and H.-C. Shin, J. Electrochem. Soc., 2010, 157, A8.

47. B. D. Adams, J. Zheng, X. Ren, W. Xu and J.-G. Zhang, Adv. Energy Mater., 2017, 8, 1702097.

48. S.-H. Hong, D.-H. Jung, J.-H. Kim, Y.-H. Lee, S.-J. Cho, S. H. Joo, H.-W. Lee, K.-S. Lee, S.-Y. Lee, Adv. Funct. Mater. 2020, 30, 1908868.

49. J. Li, P. Zou, S. W. Chiang, W. Yao, Y. Wang, P. Liu, C. Liang, F. Kang, C. Yang, Energy Storage Mater. 2020, 24, 700－706.

50. V. Pande and V. Viswanathan, ACS Energy Lett. 2019, 4, 2952－2959.

51. A. Pei, G. Zheng, F. Shi, Y. Li, Y. Cui, Nano Lett. 2017, 17, 1132－1139.

감사의 글

　지난 2년 동안 석사 학위 과정동안 도움을 주신 모든 분들께 감사의 인사드립니다. 짧다면 짧고 길다면 긴 2년간의 석사 기간 동안 힘들었던 시기도 있었지만 새로운 분야에 대한 공부와 전공 지식을 쌓을 수 있던 기간이었습니다. 문제없이 졸업 할 수 있게 도움주신 분들께 감사드립니다.

　먼저 저의 연구를 지속적으로 할 수 있게 도움을 주신 강현철 교수님, 갑작스러운 상황에 받아주시고 새로운 실험 및 공부 할 수 있게 도움 주셔서 너무나도 감사드립니다. 졸업하고 나서도 교수님 이름에 누가 되지 않도록 더욱 노력하도록 하겠습니다.

　그리고 저의 논문을 심사 해주신 이종국 교수님, 신동찬 교수님 학부 과정 때부터 교수님들의 훌륭한 강의를 듣고 전공 지식을 잘 쌓아서 잘 활용 할 수 있었습니다. 앞으로도 꾸준히 공부하고 노력하겠습니다.

　그리고 부족한 저를 받아주시고 연구를 할 수 있게 기회를 주신 이종원 교수님, 교수님 덕분에 좋은 연구와 공부를 할 수 있었습니다. 이러한 기회를 주셔서 너무나 감사드리고 앞으로도 열심히 잘 하도록 노력하겠습니다. 감사합니다.

　그리고 조선대학교 에너지소재연구실, DGIST EEMI 연구실 식구들 어색하고 잘 지낼 수 있을까 걱정도 했지만 덕분에 실험실 생활 즐겁게 했네요. 다들 무사히 학위 과정 마치고 졸업하길 바라요.

　마지막으로 학위 과정을 하는 동안 믿어주고 밀어주신 부모님 그리고 동생. 덕분에 갑작스런 타지 생활에도 걱정 없이 잘 적응 할 수 있었어요. 타지생활을 더 해야 되지만 기다려 주시고 앞으로 먼저 연락하고 자주 집에 가도록 할게요. 믿어 주셔서 감사합니다.